Production of Ξ^0 and $\bar{\Xi}^0$ hyperons by 400-GeV protons

A. Beretvas, L. Deck,* T. Devlin, K. B. Luk,† R. Rameika,‡ and P. Skubic§
Physics Department, Rutgers-The State University, P.O. Box 849, Piscataway, New Jersey 08854

P. T. Cox,** J. Dworkin,†† and O. E. Overseth
Department of Physics, University of Michigan, Ann Arbor, Michigan 48109

R. Grobel,‡‡ R. Handler, L. Pondrom, M. Sheaff, and C. Wilkinson
Physics Department, University of Wisconsin, Madison, Wisconsin 53706

K. Heller
Department of Physics, University of Minnesota, Minneapolis, Minnesota 55455

G. Bunce
Accelerator Department, Brookhaven National Laboratory, Upton, New York 11973
(Received 19 November 1985)

Inclusive production cross sections have been measured for the processes $p+A\rightarrow\Xi^0+X$ (A = Be, Cu, Pb) and for $p+\mathrm{Be}\rightarrow\bar{\Xi}^0+X$. Data were taken at angles of 0, 2, 3.5, 7.3, and 9.8 mrad between the incident 400-GeV proton beam and the outgoing hyperon beam. Production cross sections for Λ and $\bar{\Lambda}$ production were measured at the same time. The A dependence of the Ξ^0 cross sections is discussed, along with interpretations in terms of various models.

I. INTRODUCTION

A sample of 275 000 fully reconstructed decays of Ξ^0 hyperons has been collected with the Fermilab neutral-hyperon beam. A proton beam at 400 GeV incident on three different metal targets (Be, Cu, and Pb) was used to produce the neutrals at various laboratory angles between 0 and 10 mrad. These data have been analyzed to measure the asymmetry parameter[1] $\alpha(\Xi^0)$ for the decay $\Xi^0\rightarrow\Lambda\pi^0$, the Ξ^0 magnetic moment,[2] and the kinematic dependence of the Ξ^0 polarization,[3] all of which have been reported previously. In this paper invariant cross sections for the inclusive reaction $p\rightarrow\Xi^0$ are obtained by suitably correcting and normalizing the Ξ^0 momentum spectra at each production angle for each target. Early versions of these cross sections have already been discussed.[4,5]

A large flux of Λ hyperons accompanied the Ξ^0's in the neutral beam. These hyperons have been thoroughly studied. Production cross sections for Λ's by 300-GeV protons on these same metal targets were measured by Skubic *et al.*,[6] while Heller *et al.*[7] discussed the A dependence. In this experiment the Λ's were used to check the consistency of the 400- and 300-GeV production data and to normalize the Ξ^0 cross sections by a comparison with Ref. 6. The polarization of these Λ's is described in Ref. 3.

In addition cross sections have been extracted for $p\rightarrow\bar{\Lambda}$ and $p\rightarrow\bar{\Xi}^0$ production on beryllium.

The results for the $p\rightarrow\Xi^0$ cross sections are compared to two quite different models for inclusive production: the triple-Regge model and the quark-recombination model. The first approach relates inclusive cross sections to the wealth of exclusive two-body Regge phenomenology,[8] while the second employs current-quark structure functions within the incident proton to describe the shape of the spectrum of forward-moving hadrons.[9] Each model enjoys some degree of success. The triple-Regge picture has been used previously to analyze the 300-GeV production data.[10] Fits of the spectra at transverse momentum $p_t=0$ to a Feynman-x dependence which behaves as the power law $(1-x)^F$ gave exponents F which are compared to the predictions of the constituent-interchange model of Blankenbecler and Brodsky.[11]

The dependence of Ξ^0 production on the atomic weight A is also discussed by analyzing the differences in the cross sections from the three targets. Forward-moving hadrons are attenuated in nuclear matter, an effect which is much the same for a wide variety of different final-state particles.[12] The behavior of Ξ^0's is similar to that of Λ's, K_S^0's, and $\bar{\Lambda}$'s. A quark model in which quarks are "wounded" in passing through the nucleus has been applied to forward Λ production data by Bialas and Bialas[13] and Dar and Takagi.[14] Takagi[15] has used this picture to describe the A dependence of the Ξ^0 production cross sections reported here. Recently Hwa[16] has proposed using the collision function of Ref. 7 on the quarks themselves rather than the baryons, an approach which in principle allows the calculation of the A-independent functions of Takagi. Although some inconsistency remains, a simple application of this idea to the combined A-dependence data for $p\rightarrow\Lambda$, $p\rightarrow\Xi^0$, $p\rightarrow K_S^0$, and $p\rightarrow\bar{\Lambda}$ works reasonably well.[17]

The experimental apparatus is briefly described in Sec. II, while Sec. III discusses the data analysis. A discussion of the results and comparisons with various models are presented in Sec. IV.

II. EXPERIMENTAL METHOD

The essential ingredients for this measurement are a proton beam with flux monitoring, a production target, a hyperon-beam channel, and detection apparatus for the hyperon decay products. This apparatus has been described previously in Refs. 1–3 and 6.

A. Proton beam

A proton beam diffractively scattered from a beryllium target in the Meson Laboratory at Fermilab at an angle of about 0.5 mrad was transported at 400 GeV down the M2 beam line for 425 m to the second target, where the hyperons were produced. The proton beam was operated at intensities which ranged from 10^8 per accelerator cycle at 0-mrad production to 2×10^9 protons per cycle at 10 mrad. Figure 1 shows the magnetic deflection system (M_0 and M_1) used to vary the hyperon production angle, and the proton beam monitoring apparatus in the vicinity of the hyperon production target.

The proton flux and position were monitored by two ion chambers in series. One, segmented into wires 1 mm apart [a segmented-wire ion chamber (SWIC)], was used for position and spot size measurement. The beam was approximately 3 mm high and 3 mm wide, and it varied by ±1 mm in each dimension with changing conditions in the accelerator's extraction channel. The other chamber collected on a precision capacitor the total amount of charge created by the beam in 4 cm of argon gas at atmospheric pressure. The voltage across the capacitor, proportional to the total number of protons per pulse, was measured by an electrometer. The calibration constant, determined at low rates by comparison to scintillation counters was 1.3×10^7 protons/V.

B. Production targets

The hyperon production targets were all 6.35-mm-diam metal cylinders nominally $\frac{1}{2}$ interaction length thick. Actual thicknesses in gm/cm^2 were 28.3 for Be, 41.6 for Cu, and 55.8 for Pb. These same targets were used in Ref. 6.

C. Hyperon-beam channel

The neutral beam containing the hyperons was defined by a 4-mm-diam hole 3.2 m from the target ($\Delta\Omega=1.2\times10^{-6}$ sr) which was in the center of a collimator system embedded in a 5.3-m-long magnet (M_2) run at

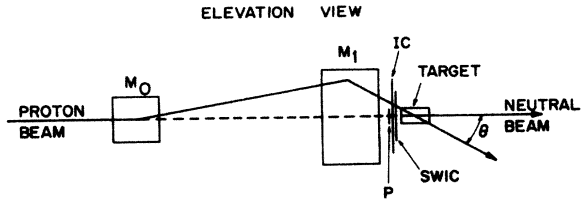

FIG. 1. Incident-proton-beam deflection system for changing the hyperon production angle and the proton beam monitors.

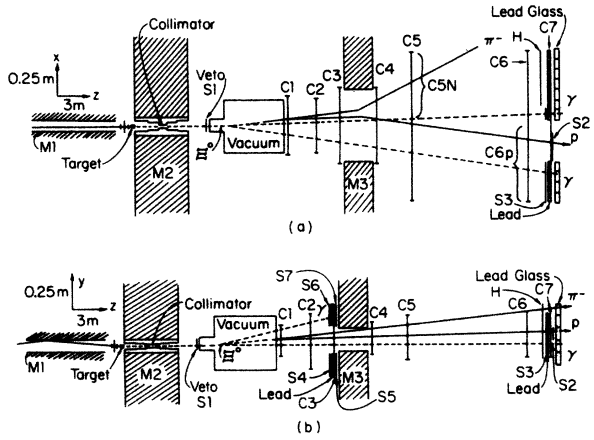

FIG. 2. (a) Plan and (b) elevation views of the hyperon-beam channel, decay volume, and downstream detection system for $\Xi^0\to\Lambda\pi^0$ decay.

2.5 T. Two views of the collimator and downstream detection system are shown in Fig. 2.

D. Detection of charged decay products

The decay of the Ξ^0 hyperon was reconstructed from observation of all of the decay products: $\Xi^0\to\Lambda\pi$, $\Lambda\to p\pi^-$, $\pi^0\to\gamma\gamma$. The proton and π^- were detected by an arrow of multiwire proportional chambers (MWPC's) with 2-mm wire spacing and an analyzing magnet (M_3) with an aperture 20 cm high, 60 cm wide, and 1.83 m long. The performance of this apparatus for $\Lambda\to p\pi^-$ has been described in detail in Ref. 6. The full width at half maximum of the Λ mass peak was 6 MeV/c^2 at 200 GeV, and narrowed slightly for lower momentum Λ's. The decays $K_S^0\to\pi^+\pi^-$ were also detected and used to determine precisely the M_3 field integral -0.960 ± 0.002 GeV/c, at 1.8-T central field by adjusting its value to yield the proper K_S^0 mass.

E. Gamma-ray detector

At least one γ ray from π^0 decay was required to shower in an array of 70 blocks of lead glass each of dimensions 100 mm $\times$100 mm $\times$384 mm (12 radiation lengths). Three blocks in the medium plane immediately to the right of the neutral beam line were removed to allow the protons from Λ decay to pass through unscathed. The block on the neutral beam was displaced behind the lead-glass array. In front of the glass there were, going upstream in order, a 30 cm$\times$10 cm proton scintillation counter S_2, a 128 cm$\times$60 cm MWPC (C_7), a 1-cm-thick lead sheet with a 40 cm$\times$10 cm hole in it to match the missing glass blocks and the recessed beam block, a veto counter (S_3) with a similar hole, and an x-y hodoscope to detect π^- from Λ decay which struck the glass. This setup is shown in exploded view in Fig. 3. About 75% of the γ rays observed in the lead glass converted in the upstream lead sheet and were detected in C_7, giving better position information for the reconstruction of those events.

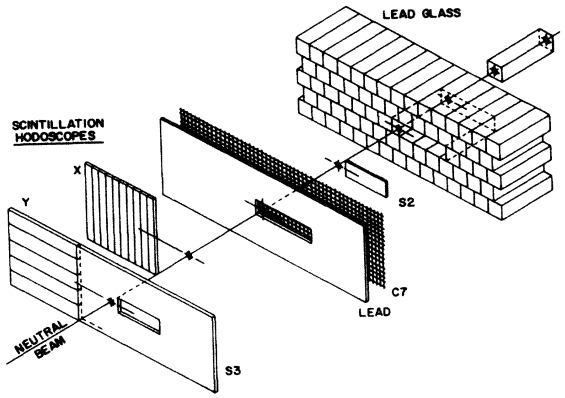

FIG. 3. Exploded view of the detection apparatus near the lead-glass array.

The second γ ray could either shower in the system described above (a G_2 event), or convert in one of the scintillator-lead-MWPC-scintillator arrays above and below the front face of the M_3 magnet aperture, shown in Fig. 2(b) (a G_1 event). Thus, both G_1 and G_2 Ξ^0's had two detected γ rays, but the energy of one γ ray was unknown for the G_1 category.

A fast parallel electronic pattern unit, the gamma cluster logic, detected γ-ray shower clusters in the lead glass for triggering purposes. The pion hodoscope information was used to remove from the cluster inventory any energy that could be assigned to an incident charged hadron rather than a photon. The operation of this pattern unit is described in more detail in Ref. 1. Two outputs L_1 (at least one cluster) and L_2 (at least two clusters) were then used in the trigger logic.

The primary energy calibration of the lead glass was performed in special runs with e^+e^- pairs. To do this a $\frac{1}{3}$ radiation length lead sheet was placed downstream of the veto counter S_1 and a second counter in coincidence was placed immediately downstream of the lead. A vertical vernier magnet near the lead converter plus the analyzing magnet M_3 spread the electrons over the glass. Three such calibration runs were made during the course of the experiment. The $\Xi^0 \rightarrow \Lambda\pi^0$ events themselves were used as a running monitor on the stability of the calibration because G_2 events were kinematically overconstrained. This check from the reconstructed data together with light pulser data served to interpolate between the pair calibration runs.

F. The trigger

There were three types of triggers. The first, which indicated a neutral V topology (predominantly $\Lambda \rightarrow p\pi^-$), was $T(\Lambda)=\bar{S}_1 \cdot C_1 \cdot C_{5N} \cdot C_{6P} \cdot S_2$, where the scintillators and chambers are shown in Fig. 2. C_{5N} was the negative-particle side of C_5, while C_{6P} was the positive-particle side of C_6. This coincidence was used as an input for the other triggers, and was allowed to trigger the data readout by itself when scaled down by a factor 128. The signatures for two detected γ rays were $G_2=\bar{S}_3 \cdot L_2$ for both of the γ rays in the glass, or $G_1=\bar{S}_3 \cdot L_1 \cdot (\bar{S}_4 \cdot S_5$ or $\bar{S}_6 \cdot S_7)$ for one in the glass and one in C_3. The Ξ^0 trigger was $T(\Xi^0)=T(\Lambda) \cdot (G_1$ or $G_2)$. $T(\Xi^0)$ and $T(\Lambda)/128$ initiated the transfer of all the MWPC coordinate data and the pulse heights from each lead-glass block to the computer for off-line analysis.

Typical trigger rates were about 400 events over the 1-sec spill time of the accelerator. In between spills pedestal and light pulser data were taken for the lead glass, and monitor scaler information, including the ion-chamber voltage, were recorded.

G. Data runs

Data were taken at five laboratory production angles with nominal values of 0, 2, 3.5, 7.3, and 9.8 mrad as determined by the excitations of M_0 and M_1 in Fig. 1. At each angle the sign of the cross product $\mathbf{k}_{in} \times \mathbf{k}_{out}$ (where $\mathbf{k}_{in}$ and $\mathbf{k}_{out}$ are the momenta of the incoming proton and outgoing hyperon) was periodically reversed to cancel apparatus effects in the measurement of hyperon polarization[3] and magnetic moment.[2] In addition, the magnitude and sign of the excitation of M_2 was also varied to change the magnetic moment precession angle. About half of the total data came from the 7.3-mrad runs, because of the emphasis on hyperon polarization found at larger production angles. Similarly, two-thirds of the data came from the Be target, with the remainder split equally between Cu and Pb.

To obtain $\bar{\Lambda}$'s from $\bar{\Xi}^0$ decay the magnetic field of the spectrometer magnet M_3 was reversed, but all other running conditions remained the same. Only Be-target data were taken in this mode, and two-thirds of this running was done at 7.3 mrad.

A typical run consisted of a single magnetic tape with 80 000 events which required about two hours of beam time. The incident proton beam intensity was adjusted as the production angle was varied to keep the trigger rates approximately the same. A total of 135 tapes were used in this analysis, of which 80 were Ξ^0 triggers, 22 were "empty" tapes with no target in the proton beam for background studies, 12 were for lead-glass calibration and chamber alignment, and 21 were $\bar{\Xi}^0$ runs.

III. ANALYSIS

A. Event selection

The event populations on a tape of Ξ^0 triggers at 7.3 mrad were typically 30% Λ triggers, 30% G_1 Ξ^0's, and 40% G_2 Ξ^0's. About 70% of the Λ triggers and 60% of the Ξ^0 triggers contained a pair of oppositely charged particles in the spectrometer which formed a V. In turn, about 60% of the V's satisfied the $\Lambda \rightarrow p\pi^-$ mass hypothesis. All events for which $M(p,\pi)=M_\Lambda \pm 3\sigma$, where the uncertainty was calculated for each event from the geometrical fit, were accepted. The trigger mixture on a 7.3-mrad $\bar{\Xi}^0$ tape was 17% $\bar{\Lambda}$, 21% G_1, and 62% G_2. The V's in this trigger were predominantly $K_S^0 \rightarrow \pi^+\pi^-$.

The hit pattern in the lead glass was studied for each trigger with a valid Λ. Calibration constants obtained from the e^+e^- calibration runs were used to convert digitized pulse height in each block to energy, and clusters were formed. No showers exclusively in blocks neighboring the neutral beam were accepted, nor were showers within 15 cm of either the projected hit of a charged pion, or another γ-ray shower. Showers composed of a very large number of blocks, which could not be of electromagnetic origin, were also rejected.

In the 7.3-mrad data about 20% of the G_2 triggers had no identified γ-ray showers which passed all of the shower criteria, 30% had one, 30% had two, and the rest had three or more. For the G_1 triggers, 25% had no acceptable shower, and 50% had one, while for the Λ triggers 45% had none and the rest had one.

Since the Ξ^0/Λ ratio in the neutral beam was in fact about 1/30, and since the detection efficiency for at least one γ ray from Ξ^0 decay was about 30%, the presence of appreciable lead-glass activity in the Λ triggers was evidence for γ-ray background not associated with Ξ^0 decays. Possible contribution of this background to the final Ξ^0 data sample is discussed below and in Ref. 1.

B. Reconstruction

The fitting procedure is described in some detail in Ref. 1. A right-handed coordinate system was defined with its origin at the collimator output of M_2, with z directed along the average neutral beam direction and (x,y) transverse to the beam, with y directed vertically upwards. Each Ξ^0 candidate with a Λ and two γ-ray conversions was fit first using only the Λ momentum vector, and the (x,y) coordinates of the two γ rays. In this fit the Ξ^0 mass and the π^0 mass were constraints, and the Ξ^0 momentum vector was allowed to vary such that the decay vertex moved along the line defined by the Λ momentum vector to obtain the best value of χ^2. For a given decay point there were three unknowns, $E_{\gamma 1}$, $E_{\gamma 2}$, and E_Ξ, resulting in a one-constraint fit to either G_1 or G_2. About 17% of the G_1 triggers and 11% of the G_2 triggers had satisfactory χ^2 fits to the decay hypothesis at this stage. The calculated γ-ray energies which correspond to showers in the lead glass were used as a running check on the gain stability of the shower detector. These events were then re-fit using the lead-glass calibration energies, giving a three-constraint fit for the G_2 Ξ's, and a two-constraint fit for the G_1's. The χ^2 distributions were cut at $\chi^2<30$ for G_2 and $\chi^2<20$ for G_1. Plots of these distributions are shown in Ref. 1. The cuts eliminated 7% of the G_1's and 10% of the G_2's. Such large data fractions at high χ^2 were not consistent with expectations from Gaussian errors, and were attributed to non-Gaussian errors associated with the γ-ray showers.

Other cuts were applied to the final data sample. Events were eliminated if they contained charged-particle trajectories close to the physical apperatures of the apparatus, or a fitted γ-ray energy in C_3 less than 1 GeV, or a fitted energy in the glass less than 3 GeV. The Λ decay vertex was required to be within the vacuum pipe, $1.9<z_\Lambda<13.0$ m, and the Ξ^0 vertex 0.6 m $<z<z_\Lambda$.

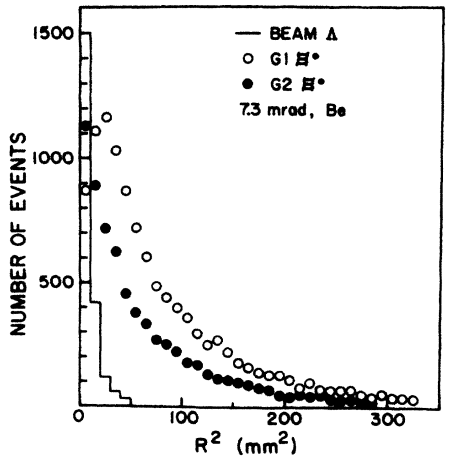

FIG. 4. Daughter and beam Λ target pointing distributions for 7.3-mrad Be target with all of the final cuts made to the data.

Many kinematic distributions were studied to assess the background remaining in the Ξ^0 data sample. Figures 4 and 5 show two such distributions at 7.3 mrad, the daughter and beam Λ target pointing distributions, and decay vertex distributions. Since the predominant background was assumed to come from beam Λ's mixing with random hits either in the glass or in C_3, comparisons of these variables, which look quite different for the two cases, were useful in estimating backgrounds. Another method, discussed in detail in Ref. 1, involved mixing the γ rays from one event with the Λ from another, and then fitting these uncorrelated events to the Ξ^0 hypothesis. The result of all of these tests was that the background in the data samples at 3.5, 7.3, and 9.8 mrad was at most 1%, and could be ignored. The 0- and 2-mrad data, where the Ξ/Λ ratio was least favorable, required an additional cut to reduce the background to this level. At these angles, events with daughter Λ target pointing $R^2<30$ mm^2 were rejected.

After all cuts a typical 7.3-mrad run yielded about 3500 events. The total numbers of events for each target and

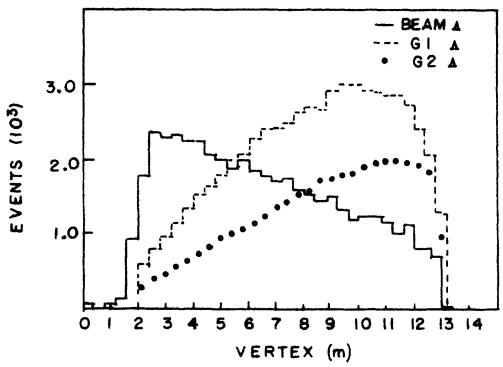

FIG. 5. Daughter and beam Λ decay vertex distributions for 7.3-mrad Be target with all of the final cuts made to the data.

TABLE I. Number of events collected with various targets and production angles.

Angle (mrad)	0.0	2.0	3.6	7.3	9.8	All angles
$p+\text{Be}\to\Xi^0+X$	10198	3729	20859	65260	48258	148304
$p+\text{Cu}\to\Xi^0+X$	9456	5101	14918	16058	19525	65058
$p+\text{Pb}\to\Xi^0+X$	9121	5201	16365	17161	14768	62616
Total Ξ^0	28775	14031	52142	98479	82551	275978
$p+\text{Be}\to\bar{\Xi}^0+X$	388	852	1742	6669		9661
$p+\text{Be}\to\Lambda+X$	69372	22159	68991	148645	108030	417197
$p+\text{Cu}\to\Lambda+X$	47980	22919	40343	32598	39868	183708
$p+\text{Pb}\to\Lambda+X$	43880	21389	41024	34619	30977	171889
Total Λ	161232	66467	150358	215862	178875	772794
$p+\text{Be}\to\bar{\Lambda}+X$	387	1020	1753	7659		10819

production angle are shown in Table I. These numbers are not the same as those listed in Table I of Ref. 1, even though the data sample is basically identical. The events used in the polarization measurements were subjected to a slightly different cuts because of the delicate nature of the asymmetry analysis. Beam Λ's were also reconstructed and retained for the normalization procedure to be explained in Sec. III D.

The $\bar{\Xi}^0$ data set was considerably smaller than the Ξ^0 set. Because of the large $K_S^0\to\pi^+\pi^-$ contamination in the $\bar{\Lambda}$ sample, it was necessary to restrict $\bar{\Lambda}$'s to those events where the two hypotheses yielded $M(\bar{p},\pi)=M_{\bar{\Lambda}}\pm 3\sigma$ and $M(\pi,\pi)\neq M_K$. This cut eliminated some $\bar{\Lambda}$'s, a loss which was included in the acceptance Monte Carlo data. Other than this difference, the $\bar{\Xi}^0$ sample was treated much like the Ξ^0. Since the $\bar{\Xi}^0/\bar{\Lambda}$ ratio was 1/10, random backgrounds of the type studied in the $\bar{\Xi}^0$ case were not as important as they were for Ξ^0. The yield at 7.3 mrad was about 1500 events per tape. The breakdown of the final sample of 9661 events is shown in Table I.

C. Corrections to the reconstructed momentum spectra

Figures 6 and 7 show the reconstructed momentum spectra for G_1 and G_2 events from the Be target at 7.3 and 0 mrad, respectively. The average Ξ^0 momentum decreased slowly with increasing angle. Spectra from the Cu and Pb targets were very similar, but the shapes at the smaller production angles decreased more sharply with increasing momentum in the heavy targets. This is illustrated in Fig. 8, which shows Be and Pb spectra normalized to correspond to measured differential multiplicity: $(1/\sigma)d\sigma/dp$.

The reconstructed Ξ^0 data consisted of 15 momentum spectra: three targets at each of five angles. Fifteen reconstructed beam Λ spectra were also obtained. There were four spectra for $\bar{\Xi}^0$ production from Be, at 0, 2, 3.5, and 7.3 mrad.

Figure 9 shows the results of a Monte Carlo study of the detection efficiency of the apparatus for $\Lambda\to p\pi^-$ decay as a function of Λ momentum, including the decay loss in the magnetic channel, the decay factor in the vacuum pipe, the geometrical efficiency for detecting the two charged particles in the spectrometer, and the probability that the proton hit the $S2$ counter (see Fig. 2). The low-momentum falloff is due to decays in the magnetic channel, an extra factor of 10 at 60 GeV/c, while the decay requirement before the end of the 10-m-long vacuum pipe caused the decrease at high momenta. The geometrical acceptance for a 150-GeV/c Λ which decayed in the vacuum was over 80%. The acceptance depended on production angle only through the change in momentum spectrum.

Figure 10 shows the companion curves for the overall detection efficiency for the sequence $\Xi^0\to\Lambda\pi^0$, $\pi^0\to\gamma\gamma$, and $\Lambda\to p\pi^-$, where either both γ's registered in the lead glass (G_2) or one γ hit the ($\bar{S}_4\cdot S_5$) or ($\bar{S}_6\cdot S_7$) counters (G_1). The sharp drop at low Ξ^0 momenta, similar to Fig. 9, is due to Ξ^0 decay loss in the collimator system. The high-momentum behavior of the G_1 and G_2 curves is dominated by the parent-daughter decay $\Xi^0\to\Lambda\to p\pi^-$

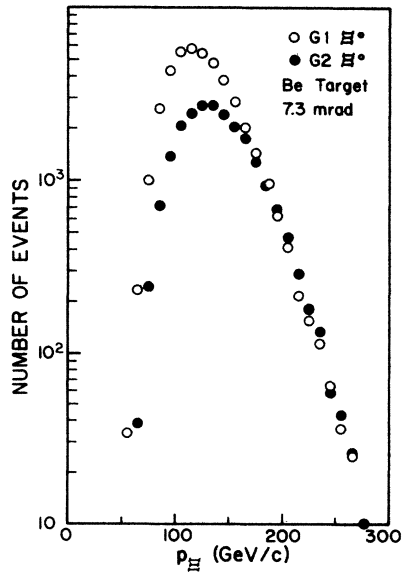

FIG. 6. Reconstructed Ξ^0 momentum spectra for G_1 and G_2 events at 7.3-mrad production from the Be target.

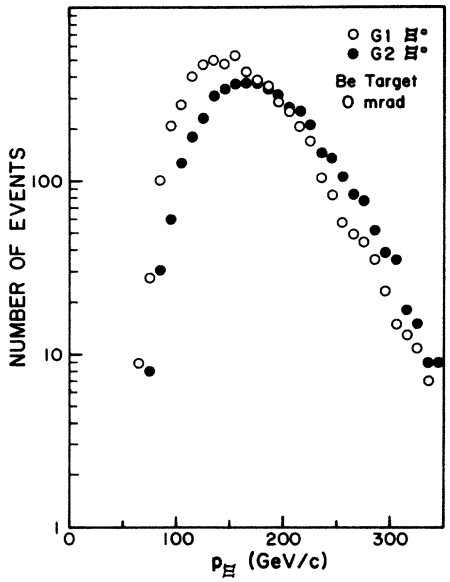

FIG. 7. Reconstructed Ξ^0 momentum spectra for G_1 and G_2 events at 0-mrad production from the Be target.

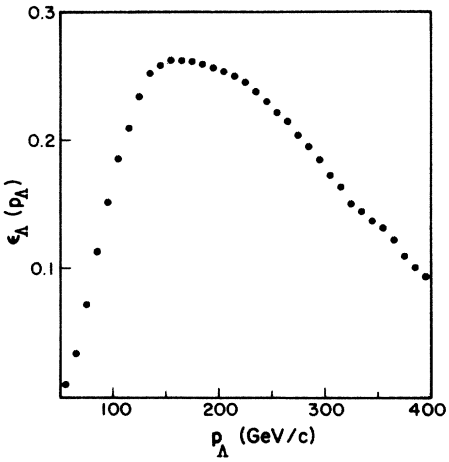

FIG. 9. Monte Carlo apparatus acceptance for $\Lambda \rightarrow p\pi^-$ as a function of Λ momentum. This curve is very similar to Fig. 9 of Ref. 6.

and by the geometrical placement of the γ-ray detectors. To a very good approximation the detection efficiency for a daughter Λ which decayed in the vacuum pipe was the same as that for a beam Λ, because their geometrical properties did not differ in a way which significantly affected the acceptance of the apparatus. Note that the peak detection efficiency for G_2 decay was about 10% of that for Λ, and that the G_1 events improved the low-momentum Ξ^0 yield substantially. The curves of Fig. 10 are correct for 3.5, 7.3, and 10 mrad, because they do not include the target pointing cut discussed in Sec. III B. Including this cut, which was applied to the 0- and 2-mrad data, decreases the efficiency by about 20%.

Dividing each momentum bin of histograms like those in Fig. 6 by the appropriate detection efficiency gave a corrected momentum spectrum shape at the production target. The Ξ^0 momentum resolution was $\Delta p/p \leq 3\%$, dominated by the uncertainties from the π^0.

One more set of corrections was applied separately to G_1 and G_2 events before curves proportional to the invariant cross sections were obtained. These corrections involved the efficiency of the electronic trigger. To determine how often a true G_1 or G_2 Ξ^0 decay was correctly identified by the trigger system, the prescaled beam Λ triggers were subjected to the Ξ^0 reconstruction analysis package. The status of the Ξ^0 detection trigger logic was recorded by fast coincidence latches for each event, so that those "beam Λ's" which were in fact Ξ^0 daughters, which had appropriate γ-ray patterns, and which reconstructed as Ξ^0 decays, could be used to determine how often the electronics would have triggered appropriately. The yield of such events was small, less than 1% of the

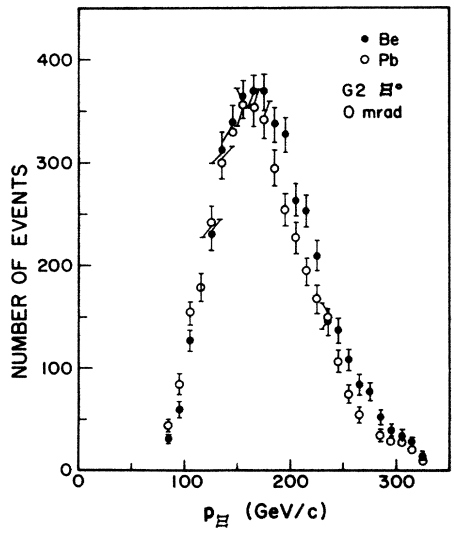

FIG. 8. Comparison of Ξ momentum spectra for G events from Be and Pb at 0 mrad. The two spectra have been normalized to correspond to measured differential multiplicity: $(1/\sigma)d\sigma/dp$.

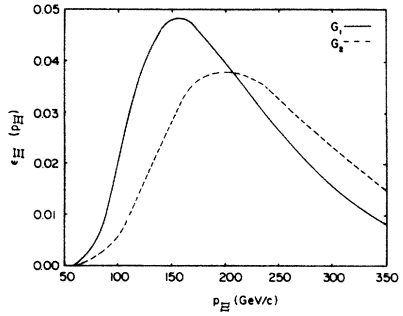

FIG. 10. Monte Carlo apparatus acceptances for the two types of $\Xi^0 \rightarrow \Lambda\pi^0$ events as functions of Ξ^0 momentum.

TABLE II. Trigger-inefficiency correction factors (ϕ).

Θ	G_2	G_1
0	1.58±0.09	2.00±0.12
2.0	1.75±0.10	2.41±0.14
3.5	1.63±0.10	2.23±0.13
7.3	1.55±0.09	2.37±0.14
9.8	1.61±0.10	2.33±0.14

(already prescaled by $\frac{1}{128}$) beam Λ triggers. Momentum- and target-independent correction factors for G_1's and G_2's were obtained in this way at each production angle. Table II shows these numbers. The errors are statistical only. The dominant part of the corrections derived from the prescaled Λ data was due to accidental counts in S_3, which would have vetoed the trigger.

Two checks on this procedure were that the yield of Ξ^0 in the beam Λ trigger sample with the correct latch pattern equaled the actual Ξ^0 yield divided by 128, and that the G_1 and G_2 spectra for a given data tape now corresponded to the same number of Ξ's produced at the target in each momentum bin.

The invariant cross sections were obtained from these numbers by applying an overall normalization factor calculated from the corrected flux of beam Λ's by a technique to be described in the next section. Figure 11 shows these invariant cross sections calculated separately for G_1 and G_2 events at 7.3 mrad, and demonstrates the level of uncertainty in the various corrections which affected the two types of events differently. The shapes are very similar, indicating that the momentum-dependent corrections to the two spectra were consistent, but the net G_1 yield is about 15% higher than the G_2, which indicates systematic uncertainty in the correction factors derived from the latch data.

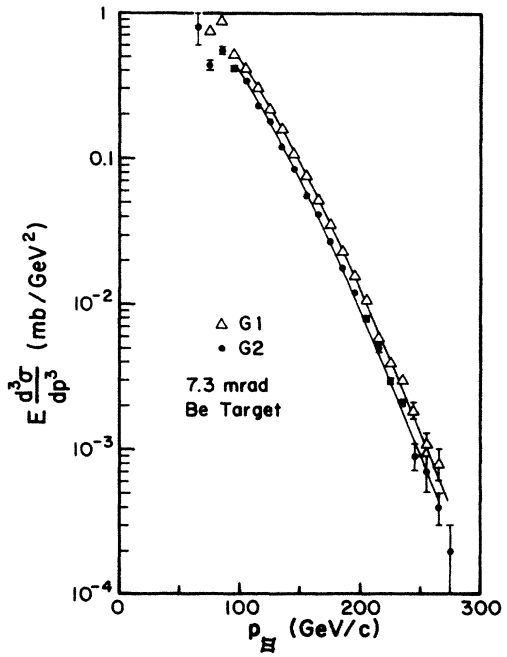

FIG. 11. Comparison of the 7.3-mrad invariant cross sections for production from Be calculated from the G_1 and G_2 events separately. The cross-section curves have the same shape within the statistical errors, but the G_1 cross section is about 15% higher than the G_2. These two results were averaged to obtain the final cross sections shown on Fig. 13.

For the other production angles and targets the agreement between the G_1 and G_2 cross sections was on the whole better than indicated by Fig. 11, although the statistical uncertainties were larger.

D. Normalization

Although the incident proton beam was monitored both in position and intensity during the course of the experiment with the apparatus shown in Fig. 1, the normalization of the Ξ^0 and $\bar{\Xi}^0$ cross sections was in fact made relative to the spectrum of beam Λ's. There were several reasons for this procedure. The proton beam intensities were higher than those used in Ref. 6, the beam-on-target efficiency was difficult to monitor, and the neutral beam collimator, being entirely of brass, did not define as sharp a solid angle as the tungsten one of Ref. 6. Thus the cross sections of Ref. 6, taken at 300 GeV, were scaled to 400 GeV and used to determine the effective proton flux for each run.

The corrected yields for Ξ^0's, $\bar{\Xi}^0$'s, and $\bar{\Lambda}$'s were converted into invariant cross sections for each tape by comparing the corrected Λ spectrum to the appropriate $p\rightarrow\Lambda$ cross section measured by Skubic *et al.*[6] This procedure is illustrated in Fig. 12, where the cross section formulas from Table VI of Ref. 6 are compared to the normalized Λ invariant cross sections from this experiment. The momentum range $100<p_\Lambda<200$ GeV/c was used to determine the normalization. As Fig. 12 shows, the spectrum shapes agree very well at 0 mrad, for $80<p_\Lambda<360$ GeV/c, and at the other angles for momenta below about 200 GeV/c, but the data of the present experiment do not fall off as rapidly with increasing p_Λ as the fit of Ref. 6 above 200 GeV/c. This discrepancy may be due to an uncertainty regarding the precise value of the angle, or to the fact that the (x,p_t) range of the present experiment is broader than that of Ref. 6. In any case, it illustrates a possible systematic error in this technique, viz., the 300-GeV data may not scale to 400 GeV.

The invariant cross section for $p+A\rightarrow\Xi^0+$ anything may be written in terms of the measured parameters as follows:

$$E\,d^3\sigma/dp^3=[N_\Xi(p_\Xi)\delta_\Xi/p_\Xi\epsilon_\Xi(p_\Xi)][C/N_{\rm at}I\,\Delta\Omega\,B\,\Delta p]\ . \tag{1}$$

Here $N_\Xi(p_\Xi)$ is the measured momentum spectrum, such as those shown in Figs. 6–8. The correction factors δ_Ξ are given in Table II. The Monte Carlo efficiencies $\epsilon_\Xi(p_\Xi)$ are plotted in Fig. 10. The factors in the second set of brackets, which are the thick-target correction C, the number of target nuclei per cm^2, $N_{\rm at}$, the proton beam flux I, the solid angle $\Delta\Omega$, the $\Lambda\rightarrow p\pi^-$ branching ratio B

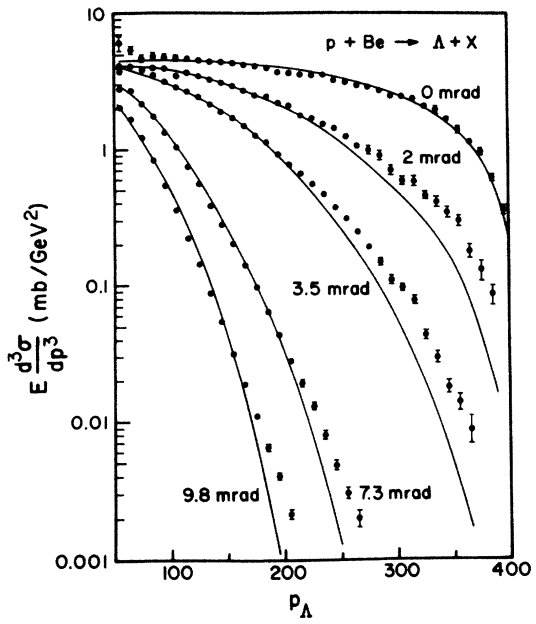

FIG. 12. Comparison of the spectra for $p+\mathrm{Be}\rightarrow\Lambda$ obtained in this experiment to the cross-section formula from Ref. 6 evaluated at the appropriate production angles at 400 GeV. This graph shows the Be target normalization technique. The momentum range $100<p_\Lambda<200$ GeV/c was used to determine the number of protons on target and the other factors common to Ξ^0 and Λ production, as discussed in the text.

$[B(\Xi^0\rightarrow\Lambda\pi^0)=1$ was assumed], and the momentum bin width Δp, were common to the Ξ^0 and Λ spectra, and were determined from the companion formula for $p+A\rightarrow\Lambda+X$: namely,

$$[C/N_{\mathrm{at}}I\,\Delta\Omega\,B\,\Delta p]=[p_\Lambda\epsilon_\Lambda(p_\Lambda)/N_\Lambda(p_\Lambda)]\times(E\,d^3\sigma/dp^3)_\Lambda\,. \quad (2)$$

The terms on the right-hand side of Eq. (2) were known independently, and this served as a check on the normalization procedure. The thick-target correction factors measured in Ref. 6 were $C_{\mathrm{Be}}=1.26\pm0.07$, $C_{\mathrm{Cu}}=1.20\pm0.07$, and $C_{\mathrm{Pb}}=1.17\pm0.07$. The number of target nuclei per cm^2, also the same as in Ref. 6, were 18.9×10^{23} for Be, 3.9×10^{23} for Cu, and 1.61×10^{23} for Pb. The solid angle $\Delta\Omega=1.15\times10^{-6}$, $\Delta p=10$ GeV/c, and $B=(0.642\pm0.005)$ (Ref. 18). The monitored proton flux for each run was compared to the calculated flux. For the 15 separate data sets (three targets and five angles) the ratio $R=$(derived proton flux)/(monitor proton flux) $=0.93\pm0.17$, where the uncertainty is the standard deviation.

A sample calculation might be useful. The raw 7.3-mrad G_2 Be spectrum for the bin centered at 145 GeV/c contained 2409 events. (See Fig. 6.) The corrected 7.3-mrad beam Λ spectrum, not shown here, gave the number of Λ's produced at the target into the solid angle of the neutral beam, which was converted via Eq. (2) to give $[C/N_{\mathrm{at}}I\,\Delta\Omega\,B\,\Delta p]=8.55\times10^{-6}$ mb/GeV, or a proton flux of 1.057×10^{13}. Including the factor $\delta=1.55$ from Table II, the momentum and the efficiency factor $\epsilon=0.026$ gives $(E\,d^3\sigma/dp^3)=0.00847$ mb/GeV^2.

The final Ξ^0 invariant cross sections were obtained by averaging the separately calculated G_2 and G_1 cross sections. The point-to-point statistical errors are the only ones given in the final results discussed in the next section. To these an overall scale uncertainty of $\pm20\%$ must be assigned to the curves due to systematic uncertainties in the corrections and procedures discussed above. The $\bar{\Xi}^0$ cross sections were treated the same way.

IV. RESULTS

A. Cross sections

Figures 13, 14, and 15 show the final results for the invariant cross sections for the reactions $p+A\rightarrow\Xi^0+$anything from Be, Cu, and Pb targets respectively, while Fig. 16 shows the cross section for $p+\mathrm{Be}\rightarrow\bar{\Xi}^0+X$. The error flags are statistical only, and do not include the overall normalization uncertainty of 20%, which applies to all data points together for each angle and target. The numbers are given in Tables III and IV.

The invariant cross sections for Λ production from Be were shown in Fig. 12 in the context of the normalization

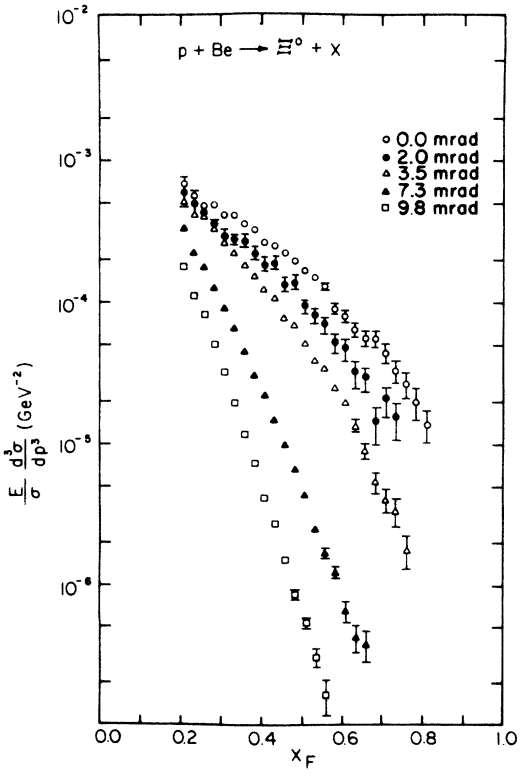

FIG. 13. Invariant cross sections for $p+\mathrm{Be}\rightarrow\Xi^0+X$ at 400 GeV at fixed production angles in the laboratory plotted as a function of $x=p/(400$ GeV/$c)$.

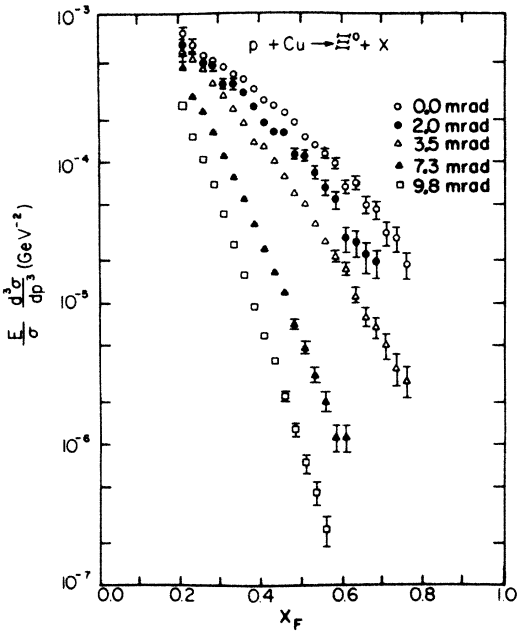

FIG. 14. Invariant cross sections for $p+\mathrm{Cu}\rightarrow\Xi^0+X$ at 400 GeV at fixed production angles in the laboratory plotted as a function of $x=p/p_{\max}$.

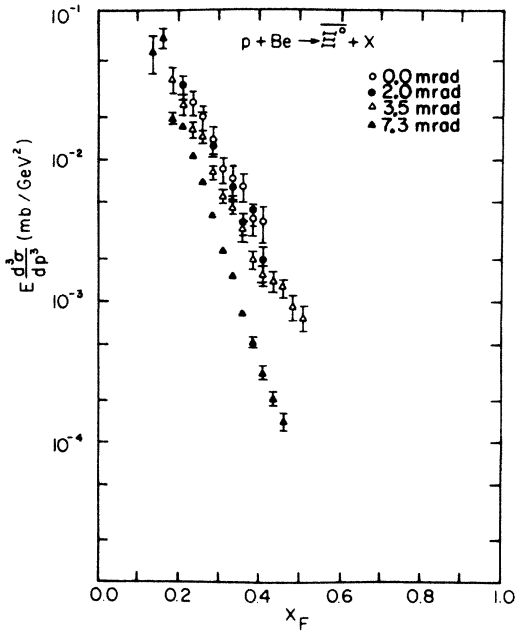

FIG. 16. Invariant cross sections for $p+\mathrm{Be}\rightarrow\bar{\Xi}^0+X$ at 400 GeV.

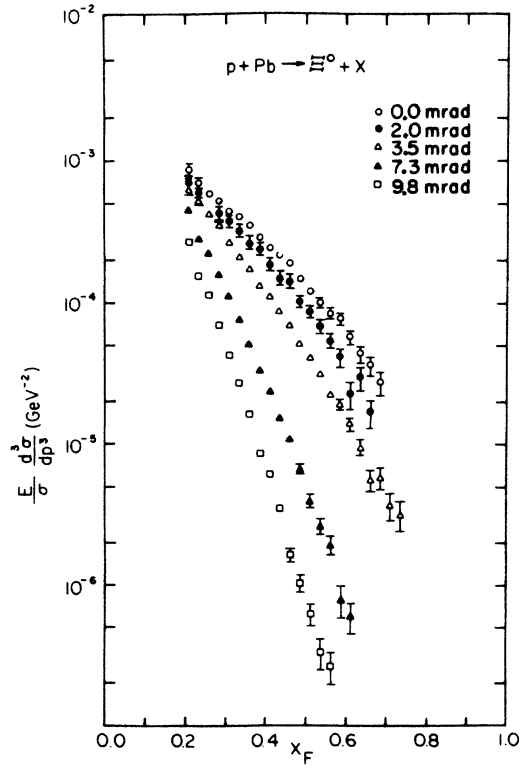

FIG. 15. Invariant cross sections for $p+\mathrm{Pb}\rightarrow\Xi^0+X$ at 400 GeV at fixed production angles in the laboratory plotted as a function of $x=p/p_{\max}$.

procedure. Companion graphs for Cu and Pb are shown in Figs. 17 and 18. The cross section for $p+\mathrm{Be}\rightarrow\bar{\Lambda}+$anything is shown in Fig. 19. The numbers are given in Tables V and VI. The overall normalization uncertainty for these data is $\pm 10\%$, smaller than for the Ξ^0's because of immunity to the γ-ray trigger-efficiency factors δ.

The ratio $\bar{\Lambda}/\Lambda$ is plotted versus $x=p/(400\ \mathrm{GeV})$ for the various laboratory angles in Fig. 20. A similar graph for the 300-GeV data is given in Fig. 26 of Ref. 6. Figure 21 shows the same plot for $\bar{\Xi}^0/\Xi^0$. In each case the ratio is approximately independent of production angle, and can be expressed as a simple exponential in x, consistent with equal numbers of antibaryons ($\bar{B}$) and baryons (B) when extrapolated to $x=0$. The slope of the $\bar{\Lambda}/\Lambda$ ratio is steeper, and the $\bar{\Xi}^0/\Xi^0$ ratio at $x=0.3$ is about three times as large as the $\bar{\Lambda}/\Lambda$. Reference 19 plots the $\bar{B}/B$ ratio for charged hyperons as a function of strangeness. Their data points are reproduced in Fig. 22 together with the extrapolated points from Figs. 20 and 21. The charged and neutral hyperon results are consistent.

In order to convert the fixed-angle invariant cross section data to smooth functions of the kinematic variables (x,p_t), an empirical fit of the same functional form used in Ref. 6 was adopted. The cross sections for each target for Ξ^0, Λ, $\bar{\Xi}^0$, and $\bar{\Lambda}$ were fit to the expression

$$E\frac{d^3\sigma}{dp^3}=\exp(C_1+C_2x^2+C_3x+C_4xp_t+C_5{p_t}^2+C_6{p_t}^4+C_7{p_t}^6)(1-x)^{(C_8+C_9{p_t}^2)}. \quad (3)$$

The values of the coefficients and the χ^2 for the fits to the Ξ^0 and $\bar{\Xi}^0$ data are given in Table VII, while those for Λ

TABLE III. Invariant cross sections in units of 10^{-28} cm^2/GeV^2 for Ξ^0 production by 400-GeV protons at various production angles.

x_F	0.0 mrad	2.0 mrad	3.5 mrad	7.3 mrad	9.8 mrad
			$p+\text{Be}\rightarrow\Xi^0+X$		
0.212	1.46±0.20	1.21±0.19	1.12±0.09	0.72±0.02	0.382±0.010
0.238	1.22±0.12	1.04±0.15	0.90±0.05	0.484±0.010	0.239±0.005
0.262	1.04±0.08	0.91±0.10	0.87±0.04	0.386±0.007	0.174±0.003
0.288	1.06±0.07	0.76±0.07	0.71±0.03	0.274±0.005	0.1093±0.0019
0.312	0.90±0.05	0.65±0.06	0.58±0.02	0.198±0.003	0.0692±0.0012
0.338	0.89±0.05	0.61±0.05	0.486±0.016	0.144±0.002	0.0418±0.0008
0.362	0.78±0.04	0.58±0.05	0.395±0.013	0.0979±0.0018	0.0251±0.0006
0.388	0.70±0.03	0.47±0.04	0.327±0.011	0.0661±0.0014	0.0157±0.0004
0.412	0.58±0.03	0.40±0.03	0.266±0.009	0.0476±0.0011	0.0088±0.0003
0.438	0.54±0.03	0.41±0.03	0.235±0.008	0.0318±0.0009	0.0059±0.0002
0.462	0.49±0.03	0.29±0.03	0.168±0.007	0.0213±0.0007	0.0032±0.0001
0.488	0.43±0.02	0.30±0.03	0.150±0.006	0.0142±0.0006	0.0019±0.0001
0.512	0.36±0.02	0.20±0.02	0.112±0.006	0.0094±0.0004	0.0012±0.0001
0.538	0.32±0.02	0.18±0.02	0.085±0.005	0.0054±0.0003	0.0007±0.0001
0.562	0.28±0.02	0.15±0.02	0.074±0.004	0.0036±0.0003	0.0004±0.0001
0.588	0.20±0.02	0.11±0.02	0.054±0.004	0.0027±0.0002	
0.612	0.17±0.02	0.10±0.02	0.043±0.003	0.0014±0.0002	
0.638	0.14±0.02	0.068±0.015	0.029±0.003	0.0009±0.0002	
0.662	0.12±0.02	0.063±0.012	0.019±0.002	0.0008±0.0002	
0.688	0.12±0.02	0.030±0.009	0.0115±0.0019		
0.712	0.096±0.015	0.044±0.011	0.0087±0.0016		
0.738	0.071±0.013	0.033±0.010	0.0072±0.0016		
0.762	0.057±0.012		0.0038±0.0010		
0.788	0.043±0.011				
0.812	0.030±0.008				
			$p+\text{Cu}\rightarrow\Xi^0+X$		
0.212	6.3±0.8	5.0±0.9	5.0±0.4	3.74±0.19	2.02±0.08
0.238	5.1±0.5	5.4±0.6	4.3±0.2	2.38±0.10	1.22±0.04
0.262	4.6±0.3	3.9±0.3	3.68±0.17	1.89±0.06	0.85±0.02
0.288	4.2±0.3	3.8±0.3	2.93±0.12	1.34±0.04	0.561±0.015
0.312	3.8±0.2	2.9±0.2	2.40±0.09	0.91±0.03	0.346±0.010
0.338	3.35±0.18	2.82±0.19	1.93±0.07	0.64±0.02	0.210±0.007
0.362	3.11±0.16	2.51±0.16	1.56±0.06	0.449±0.016	0.129±0.005
0.388	2.64±0.13	2.00±0.13	1.14±0.05	0.299±0.012	0.076±0.003
0.412	2.22±0.12	1.57±0.11	1.05±0.04	0.199±0.010	0.048±0.003
0.438	2.04±0.11	1.32±0.10	0.83±0.04	0.136±0.008	0.031±0.002
0.462	1.82±0.10	1.32±0.10	0.65±0.03	0.099±0.006	0.0178±0.0015
0.488	1.54±0.09	0.93±0.09	0.49±0.03	0.058±0.005	0.0103±0.0011
0.512	1.23±0.08	0.90±0.08	0.41±0.02	0.040±0.004	0.0060±0.0009
0.538	1.08±0.08	0.69±0.07	0.30±0.02	0.025±0.003	0.0037±0.0007
0.562	0.93±0.07	0.53±0.07	0.224±0.018	0.017±0.003	0.0020±0.0005
0.588	0.80±0.07	0.43±0.06	0.175±0.016	0.009±0.002	
0.612	0.54±0.06	0.23±0.05	0.143±0.015		
0.638	0.58±0.06	0.22±0.05	0.094±0.012		
0.662	0.40±0.06	0.17±0.04	0.065±0.010		
0.688	0.37±0.06	0.16±0.03	0.055±0.009		
0.712	0.25±0.05		0.041±0.008		
0.738	0.23±0.05		0.028±0.007		
0.762	0.15±0.03		0.023±0.006		
			$p+\text{Pb}\rightarrow\Xi^0+X$		
0.212	16.5±2.0	13.1±2.0	12.3±0.9	8.6±0.4	5.1±0.2
0.238	13.5±1.2	11.2±1.2	10.0±0.5	5.4±0.2	2.97±0.10
0.262	11.3±0.8	8.3±0.7	8.3±0.4	4.32±0.14	2.20±0.07
0.288	10.1±0.6	8.0±0.6	6.7±0.3	3.08±0.09	1.35±0.04
0.312	8.5±0.5	7.0±0.5	5.18±0.19	2.16±0.07	0.83±0.03
0.338	7.8±0.4	6.0±0.4	4.04±0.15	1.49±0.05	0.523±0.019
0.362	6.8±0.3	4.9±0.3	3.32±0.12	0.98±0.04	0.316±0.014

TABLE III. (*Continued*).

	$p+\text{Be}\rightarrow\Xi^0+X$				
x_F	0.0 mrad	2.0 mrad	3.5 mrad	7.3 mrad	9.8 mrad
0.388	5.6±0.3	4.5±0.3	2.58±0.10	0.65±0.03	0.165±0.009
0.412	4.7±0.2	3.5±0.2	2.16±0.09	0.46±0.02	0.119±0.007
0.438	4.2±0.2	2.8±0.2	1.70±0.07	0.296±0.016	0.068±0.005
0.462	3.7±0.2	2.7±0.2	1.34±0.06	0.211±0.014	0.032±0.004
0.488	2.88±0.19	1.99±0.18	1.00±0.05	0.129±0.011	0.020±0.003
0.512	2.36±0.17	1.68±0.16	0.80±0.05	0.077±0.008	0.012±0.002
0.538	1.96±0.16	1.33±0.15	0.60±0.04	0.051±0.007	0.0064±0.0016
0.562	1.65±0.15	1.05±0.13	0.43±0.04	0.038±0.006	0.0051±0.0013
0.588	1.50±0.15	0.79±0.12	0.37±0.03	0.015±0.004	
0.612	1.11±0.13	0.43±0.09	0.27±0.03	0.012±0.003	
0.638	0.84±0.12	0.57±0.11	0.18±0.02		
0.662	0.70±0.11	0.32±0.07	0.108±0.018		
0.688	0.52±0.10		0.112±0.019		
0.712			0.071±0.015		
0.738			0.062±0.014		

and $\bar{\Lambda}$ are given in Table VIII. The fits were first made to the form $e^{(C_1+C_5p_t^2)}(1-x)^{C_8}$ to force the coefficients C_5 and C_8 to account for as much of the kinematic behavior as possible. Second, C_5 and C_8 were fixed and the others in Eq. (3) varied to improve the fit. Finally, the values found in the second step were used as starting points and all coefficients were allowed to vary in improving the fit. The values changed little in the last step.

The three nuclear targets were used to perform an extrapolation to a nucleon via a power-law A-dependence hypothesis. (See Fig. 30.) For a given (x,p_t) the nucleon cross section was written in the form

$$(E\,d^3\sigma/dp^3)\,|_A = A^{\alpha(x,p)}(E\,d^3\sigma/dp^3)\,|_{A=1}\,. \qquad (4)$$

The $A=1$ cross sections obtained from this procedure were then fit to the form of Eq. (3). Coefficients of the fit to the "nucleon" spectra for Ξ^0 and Λ are also given in Tables VII and VIII. Further discussion of the A dependence appears in Sec. IV E.

B. Regge analysis

The triple-Regge behavior for inclusive production of neutral strange particles has been investigated earlier,[10] and it was found that, for inclusive Λ production, the Regge slope and intercept are consistent with $K^*(K^{**})$ exchange. Figure 23 shows the "nucleon" data from this experiment for Λ's. The data at smaller $(1-x)$ for each production angle are consistent with straight lines on a log-log plot. Where necessary, it was assumed to extrapo-

TABLE IV. Invariant cross sections in units of 10^{-28} cm^2/GeV^2 for $\bar{\Xi}^0$ production by 400-GeV protons at various production angles.

	$p+\text{Be}\rightarrow\bar{\Xi}^0+X$			
x_F	0.0 mrad	2.0 mrad	3.5 mrad	7.3 mrad
0.212		0.33±0.06	0.25±0.04	0.174±0.011
0.238	0.25±0.05	0.24±0.03	0.16±0.02	0.106±0.0052
0.262	0.20±0.04	0.19±0.02	0.147±0.016	0.071±0.0032
0.288	0.14±0.03	0.12±0.02	0.082±0.010	0.0406±0.0019
0.312	0.087±0.018	0.082±0.013	0.056±0.007	0.0232±0.0012
0.338	0.073±0.018	0.063±0.010	0.046±0.005	0.0152±0.0009
0.362	0.065±0.015	0.034±0.008	0.033±0.004	0.0084±0.0006
0.388	0.039±0.010	0.041±0.007	0.020±0.003	0.0052±0.0004
0.412	0.036±0.011	0.019±0.005	0.015±0.003	0.0032±0.0003
0.438			0.014±0.002	0.0021±0.0002
0.462			0.013±0.002	0.0014±0.0002
0.488			0.0091±0.0018	
0.512			0.0077±0.0015	

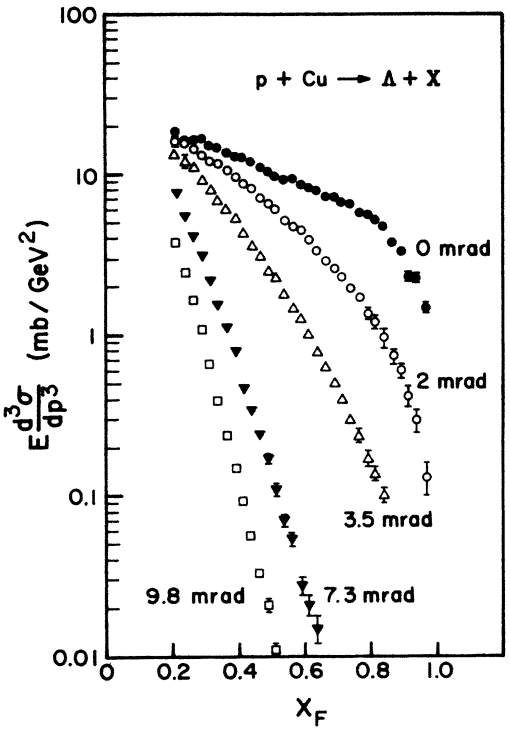

FIG. 17. Invariant cross sections for $p+\mathrm{Cu}\rightarrow\Lambda+X$ at 400 GeV. The Be cross sections are shown in Fig. 12.

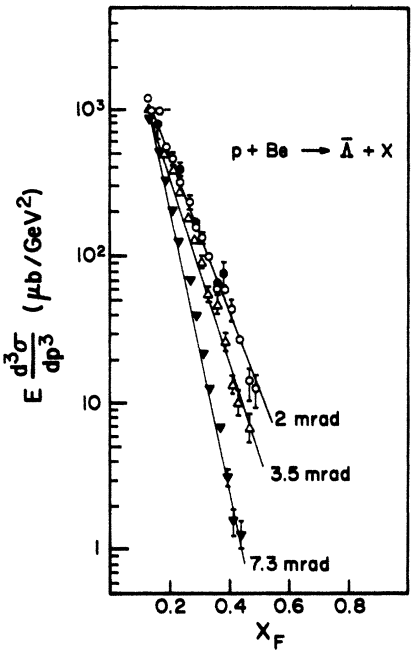

FIG. 19. Invariant cross sections for $p+\mathrm{Be}\rightarrow\bar{\Lambda}+X$ at 400 GeV.

late linearly into the triple-Regge region, $0.02<(1-x)<0.2$. In this region the cross sections should behave as

$$E\frac{d^3\sigma(x,t)}{dp^3}=\beta(t)(1-x)^{[1-2\alpha_R(t)]}, \tag{5}$$

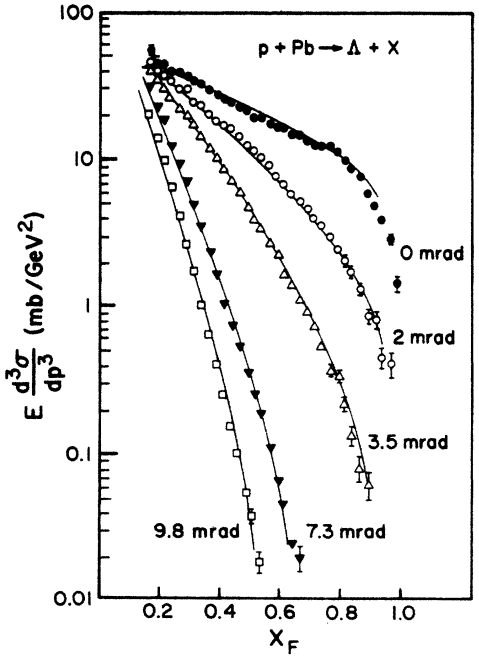

FIG. 18. Invariant cross sections for $p+\mathrm{Pb}\rightarrow\Lambda+X$ at 400 GeV. The lines are from the fitted function given in Table VIII.

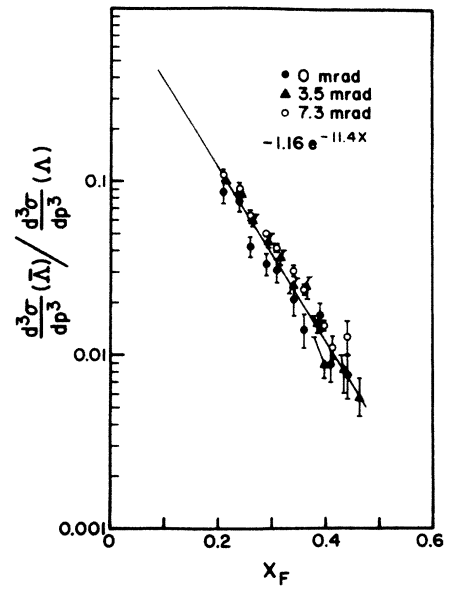

FIG. 20. $\bar{\Lambda}/\Lambda$ ratio for Be at three laboratory production angles. The line corresponds to the fit, $e^{-11.4X}$, in Ref. 6 to the 300-GeV data.

TABLE V. Invariant cross sections in units of 10^{-27} cm^2/GeV^2 for Λ production by 400-GeV protons at various production angles.

x_F	0.0 mrad	2.0 mrad	3.5 mrad	7.3 mrad	9.8 mrad
			$p+\text{Be}\rightarrow\Lambda+X$		
0.212	4.87±0.17	4.06±0.21	3.58±0.07	1.717±0.015	0.826±0.007
0.238	4.90±0.14	4.05±0.17	3.16±0.06	1.305±0.011	0.530±0.004
0.262	4.80±0.12	3.46±0.14	2.91±0.05	1.011±0.008	0.352±0.003
0.288	4.89±0.11	3.80±0.13	2.75±0.04	0.759±0.006	0.2225±0.0022
0.312	4.59±0.10	3.54±0.11	2.40±0.03	0.552±0.005	0.1415±0.0016
0.338	4.56±0.09	3.22±0.10	2.19±0.03	0.386±0.004	0.0861±0.0012
0.362	4.52±0.09	3.09±0.09	1.875±0.027	0.275±0.003	0.0526±0.0009
0.388	4.40±0.08	2.97±0.09	1.692±0.025	0.2007±0.0024	0.0313±0.0007
0.412	4.14±0.08	2.70±0.08	1.508±0.022	0.1369±0.0020	0.0191±0.0005
0.438	4.10±0.08	2.61±0.08	1.257±0.020	0.0956±0.0016	0.0114±0.0004
0.462	3.96±0.07	2.49±0.07	1.136±0.018	0.0630±0.0014	0.0065±0.0003
0.488	3.66±0.07	2.19±0.07	0.921±0.016	0.0439±0.0011	0.0040±0.0002
0.512	3.73±0.07	2.13±0.06	0.799±0.015	0.0283±0.0009	0.0023±0.0002
0.538	3.60±0.06	1.74±0.06	0.685±0.014	0.0192±0.0007	0.0014±0.0001
0.562	3.49±0.06	1.71±0.06	0.563±0.012	0.0126±0.0005	0.0008±0.0001
0.588	3.51±0.06	1.55±0.05	0.476±0.011	0.0078±0.0005	0.0004±0.0001
0.612	3.24±0.06	1.44±0.05	0.381±0.010	0.0049±0.0004	
0.638	3.08±0.06	1.25±0.05	0.310±0.009	0.0030±0.0003	
0.662	2.98±0.06	1.07±0.04	0.254±0.008	0.0020±0.0003	
0.688	2.90±0.06	0.99±0.04	0.199±0.007	0.0010±0.0003	
0.712	2.67±0.06	0.92±0.04	0.149±0.006		
0.738	2.49±0.05	0.71±0.04	0.114±0.006		
0.762	2.55±0.06	0.59±0.03	0.097±0.005		
0.788	2.37±0.05	0.57±0.03	0.078±0.005		
0.812	2.06±0.05	0.45±0.03	0.044±0.004		
0.838	1.97±0.05	0.42±0.03	0.030±0.003		
0.862	1.70±0.05	0.350±0.027	0.0179±0.0023		
0.888	1.37±0.04	0.299±0.025	0.0139±0.0021		
0.912	1.12±0.04	0.177±0.020	0.0087±0.0017		
0.938	0.96±0.04	0.130±0.018	0.0052±0.0014		
0.962	0.61±0.03	0.086±0.015			
			$p+\text{Cu}\rightarrow\Lambda+X$		
0.212	18.4±0.7	16.3±0.7	13.5±0.3	7.61±0.13	3.74±0.05
0.238	16.0±0.5	15.6±0.6	12.12±0.26	5.46±0.09	2.45±0.03
0.262	16.6±0.5	14.2±0.5	10.76±0.21	4.09±0.07	1.653±0.023
0.288	16.8±0.4	13.1±0.4	9.39±0.17	3.16±0.05	1.071±0.017
0.312	15.2±0.4	12.0±0.4	7.97±0.14	2.15±0.04	0.662±0.012
0.338	14.8±0.3	11.9±0.3	6.84±0.12	1.55±0.03	0.400±0.009
0.362	13.8±0.3	10.39±0.29	6.16±0.11	1.089±0.025	0.240±0.006
0.388	13.00±0.29	9.63±0.27	5.25±0.10	0.792±0.020	0.149±0.005
0.412	12.87±0.28	8.79±0.25	4.42±0.09	0.471±0.015	0.093±0.004
0.438	12.08±0.26	8.12±0.23	3.59±0.08	0.336±0.013	0.0578±0.0028
0.462	11.07±0.25	6.99±0.21	3.08±0.07	0.237±0.011	0.0334±0.0021
0.488	10.59±0.24	6.61±0.20	2.55±0.06	0.170±0.009	0.0215±0.0017
0.512	9.77±0.22	6.12±0.19	2.30±0.06	0.107±0.007	0.0112±0.0013
0.538	9.35±0.21	5.08±0.17	1.81±0.05	0.070±0.005	0.0069±0.0010
0.562	9.67±0.21	4.75±0.16	1.49±0.05	0.054±0.005	0.0031±0.0007
0.588	8.82±0.20	4.60±0.16	1.29±0.04	0.028±0.004	0.0025±0.0006
0.612	8.26±0.20	3.89±0.15	1.00±0.04	0.021±0.003	
0.638	8.00±0.19	3.35±0.14	0.79±0.03	0.0149±0.0025	
0.662	7.22±0.18	2.95±0.13	0.64±0.03	0.0069±0.0018	
0.688	7.26±0.18	2.58±0.12	0.490±0.026		
0.712	6.80±0.18	2.30±0.11	0.408±0.024		
0.738	6.69±0.18	1.98±0.11	0.299±0.021		
0.762	5.84±0.17	1.71±0.10	0.237±0.019		
0.788	5.69±0.17	1.36±0.09	0.170±0.016		
0.812	5.18±0.16	1.22±0.09	0.128±0.014		

TABLE V. (*Continued*).

x_F	0.0 mrad	2.0 mrad	3.5 mrad	7.3 mrad	9.8 mrad
			$p+\text{Be}\rightarrow\Lambda+X$		
0.838	4.70±0.16	0.96±0.08	0.106±0.013		
0.862	3.85±0.15	0.75±0.07			
0.888	3.36±0.14	0.60±0.06			
0.912	2.33±0.12	0.43±0.06			
0.938	2.29±0.12	0.30±0.05			
0.962	1.48±0.10	0.13±0.03			
			$p+\text{Pb}\rightarrow\Lambda+X$		
0.212	44.6±1.6	36.9±1.6	30.2±0.7	17.7±0.28	9.59±0.14
0.238	38.9±1.2	33.9±1.3	26.0±0.5	12.36±0.20	6.29±0.09
0.262	38.8±1.0	30.4±1.0	22.3±0.4	9.09±0.15	4.01±0.08
0.288	35.9±0.9	30.0±0.9	19.1±0.3	6.89±0.11	2.66±0.06
0.312	34.2±0.8	24.4±0.7	16.76±0.29	4.74±0.09	1.71±0.03
0.338	32.5±0.7	23.4±0.7	13.89±0.25	3.41±0.07	1.034±0.025
0.362	28.9±0.7	20.3±0.6	11.66±0.22	2.35±0.05	0.636±0.019
0.388	26.7±0.6	18.6±0.6	10.29±0.20	1.58±0.04	0.396±0.014
0.412	25.5±0.6	17.3±0.5	8.36±0.17	1.10±0.03	0.251±0.011
0.438	23.8±0.5	15.7±0.5	7.19±0.15	0.746±0.028	0.154±0.008
0.462	21.8±0.5	14.2±0.4	5.91±0.14	0.523±0.023	0.098±0.006
0.488	21.5±0.5	12.4±0.4	4.78±0.12	0.340±0.018	0.054±0.005
0.512	19.5±0.5	11.1±0.4	3.90±0.11	0.238±0.015	0.037±0.004
0.538	18.8±0.5	10.5±0.4	3.38±0.10	0.181±0.013	0.0177±0.0028
0.562	17.4±0.4	9.1±0.3	2.68±0.09	0.108±0.010	0.0110±0.0023
0.588	16.4±0.4	7.8±0.3	2.18±0.08	0.066±0.009	0.0083±0.0019
0.612	16.1±0.4	6.87±0.29	1.65±0.07	0.044±0.007	
0.638	14.6±0.4	5.67±0.26	1.41±0.06	0.024±0.005	
0.662	13.8±0.4	4.98±0.24	1.14±0.06	0.019±0.004	
0.688	13.2±0.4	4.55±0.23	0.90±0.05		
0.712	12.4±0.4	3.95±0.22	0.73±0.04		
0.738	12.1±0.4	3.47±0.21	0.52±0.04		
0.762	11.8±0.4	2.90±0.19	0.36±0.03		
0.788	10.9±0.4	2.41±0.18	0.33±0.03		
0.812	9.3±0.3	1.97±0.16	0.212±0.026		
0.838	8.5±0.3	1.66±0.15	0.127±0.020		
0.862	7.4±0.3	1.32±0.14	0.082±0.016		
0.888	5.72±0.27	0.85±0.11	0.062±0.014		
0.912	4.69±0.25	0.80±0.11			
0.938	3.77±0.23	0.44±0.09			
0.962	2.81±0.20	0.40±0.08			

TABLE VI. Invariant cross sections in units of 10^{-27} cm^2/GeV^2 for $\bar{\Lambda}$ production by 400-GeV protons at various production angles.

x_F	0.0 mrad	2.0 mrad	3.5 mrad	7.3 mrad
		$p+\text{Be}\rightarrow\bar{\Lambda}+X$		
0.212	0.43±0.06	0.46±0.04	0.382±0.025	0.196±0.006
0.238	0.38±0.05	0.310±0.029	0.276±0.018	0.120±0.004
0.262	0.20±0.03	0.229±0.022	0.180±0.012	0.0665±0.0025
0.288	0.165±0.027	0.163±0.016	0.129±0.009	0.0382±0.0016
0.312	0.142±0.023	0.134±0.014	0.089±0.007	0.0226±0.0012
0.338	0.097±0.018	0.097±0.011	0.054±0.005	0.0124±0.0008
0.362	0.063±0.014	0.058±0.008	0.048±0.005	0.0065±0.0006
0.388	0.076±0.015	0.056±0.008	0.026±0.003	0.0030±0.0004
0.412	0.038±0.010	0.042±0.006	0.0134±0.0023	0.0015±0.0003
0.438	0.032±0.009	0.026±0.003	0.0104±0.0026	0.0012±0.0003
0.462		0.013±0.004	0.0067±0.0016	
0.488		0.012±0.003		

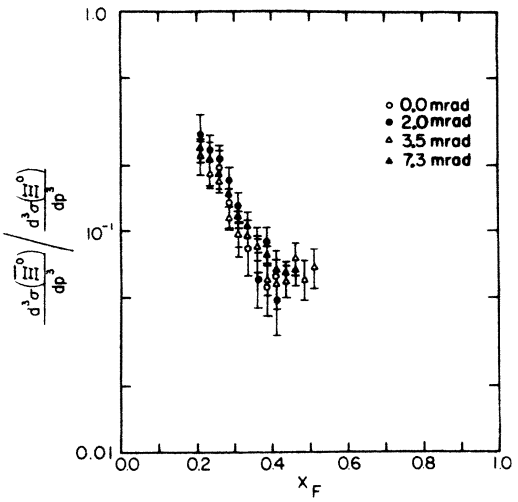

FIG. 21. $\bar{\Xi}^0/\Xi^0$ ratio for Be at four laboratory production angles.

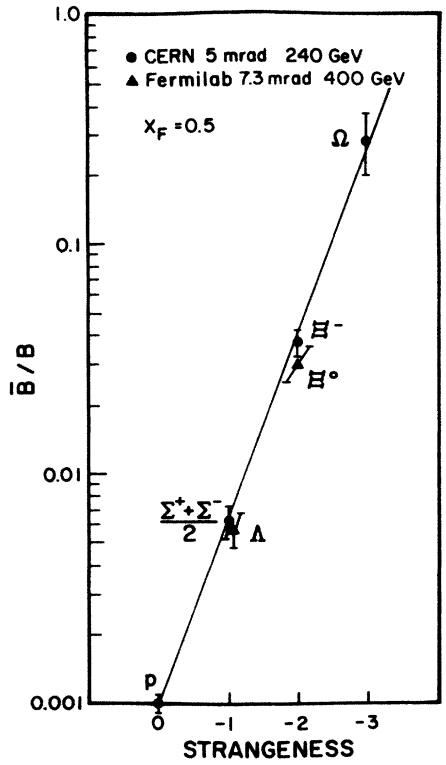

FIG. 22. $\bar{B}/B$ ratio as a function of strangeness, with the results for neutral hyperons from this experiment (Fermilab) compared to the charged-hyperon results from Ref. 19 (CERN).

whereas the data approach the behavior

$$E\frac{d^3\sigma(x,\theta)}{dp^3}=b(\theta)(1-x)^{[1-2s(\theta)]} \tag{6}$$

for fixed θ as $(1-x)\to 0$. For small values of $1-x$, t is proportional to θ^2 and it is a simple matter to relate the observed behavior of Eq. (6) to Eq. (5). Figure 24 shows a Chew-Frautschi plot of $\alpha_R(t)$ vs t for Λ production which is similar to the results of Ref. 10.

A similar analysis of the Ξ^0 data is given in Figs. 25 and 26. If all points plotted in Fig. 26 are fit with a straight line, we find

$$\alpha_R(t)=-0.67+0.39t\ . \tag{7}$$

If only the three points closest to $t=0$ are used, then

$$\alpha_R(t)=-0.59+0.49t\ . \tag{8}$$

In this process, $p\to\Xi^0$, two units of strangeness must be exchanged, i.e., a state with exotic quantum numbers is required. Since no exotic mesons are known to exist, the simplest state available is K^*K^*, a cut singularity in the complex angular momentum plane. For such a cut $\alpha_C(t)$ resulting from two poles $\alpha_P(t)$ we expect the slope and intercept to be, respectively,

$$\alpha_C'(0)=\alpha_P'(0)/2=0.45\ , \tag{9}$$

$$\alpha_C(0)=2\alpha_P(0)=-0.5\ . \tag{10}$$

The data are consistent with these values.

The phenomenology of Regge cuts in various processes

TABLE VII. Ξ^0 and $\bar{\Xi}^0$ fits. DF means number of degrees of freedom.

		Ξ^0			$\bar{\Xi}^0$
Parameter	Nucleon	Be	Cu	Pb	Be
C_1	−1.16±0.01	−1.15±0.01	0.70±0.01	1.65±0.08	0.21±0.03
C_2	1.73±0.09	1.76±0.06	3.16±0.04	3.61±0.61	17.4±0.3
C_3	−0.80±0.04	−0.94±0.01	−2.09±0.02	−1.84±0.32	−7.49±0.09
C_4	−1.03±0.03	−0.96±0.04	−1.31±0.02	−2.04±0.09	−5.63±0.13
C_5	−1.69±0.01	−1.69±0.02	−1.48±0.01	−1.26±0.01	−1.58±0.06
C_6	0.083±0.005	0.103+0.004	0.068±0.002		−1.79±0.11
C_7					
C_8	3.08±0.01	3.00±0.01	3.52±0.01	4.17±0.11	11.0±0.1
C_9	−0.27±0.02	−0.14±0.03	−0.30±0.01	−0.57±0.03	8.27±0.06
Data points	93	104	97	93	41
χ^2/DF	1.37	1.33	0.92	1.03	0.84

TABLE VIII. Λ and $\bar{\Lambda}$ fits, DF means number of degrees of freedom.

Parameter	Nucleon	Λ Be	Λ Cu	Λ Pb	$\bar{\Lambda}$ Be
C_1	1.62±0.01	1.67±0.02	3.44±0.02	4.46±0.01	1.21±0.05
C_2		0.44±0.14	1.96±0.17	2.98±0.08	
C_3	0.52±0.04	0.28±0.08	−1.79±0.07	−2.81±0.01	
C_4	−0.67±0.01	−0.58±0.05	−0.92±0.05	−1.73±0.06	
C_5	−2.58±0.01	−2.62±0.02	−2.21±0.01	−1.92±0.03	−2.34±0.04
C_6	0.360±0.002	0.40±0.01	0.31±0.01	0.30±0.02	
C_7	−0.028±0.001	−0.033±0.003	−0.023±0.002	−0.025±0.003	
C_8	0.77±0.02	0.86±0.04	0.99±0.05	1.06±0.03	8.4±0.2
C_9	0.29±0.01	0.20±0.02	0.12±0.03	0.07±0.03	
Data points	125	128	123	125	43
χ^2/DF	2.07	2.45	2.11	1.55	1.11

is discussed by Collins.[8] The properties of exotic exchanges in two-body exclusive processes, such as $K^-p \to K^+\Xi^-$, must be deduced from the s dependence. There are hints of cut behavior in such reactions, but clear evidence is difficult to obtain because the cross sections for such processes are "too small to measure except near threshold."[8]

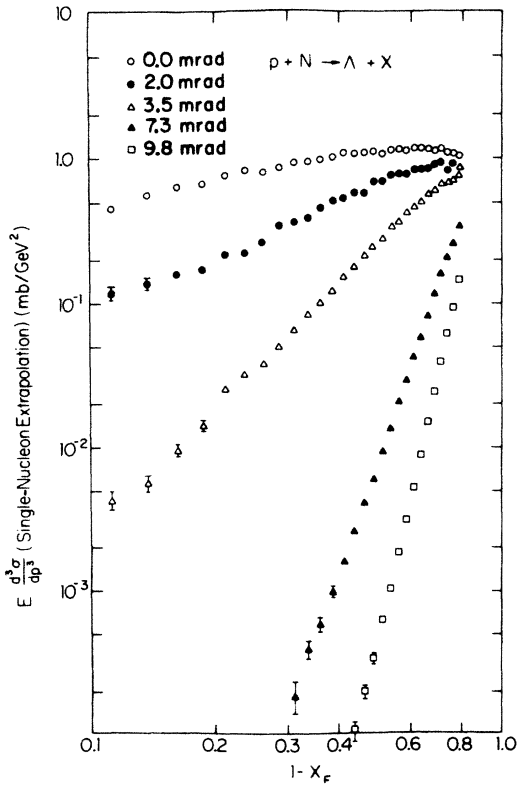

FIG. 23. Invariant cross sections for Λ production from the "nucleon" target, obtained by extrapolation of the complex nuclear cross sections to $A=1$ via Eq. (4), in a logarithmic plot vs $(1-x)$, for fixed production angle, illustrating the behavior $b(\theta)(1-x)^{[1-2a(\theta)]}$ of Eq. (6). The approximate linearity for small values of $(1-x)$ suggests triple-Regge behavior.

In order for an exotic meson to provide a significant pole contribution to the reaction studied here, its coupling strength would have to be comparable to that of the observed cut, and its Regge trajectory would have to lie above that of Eq. (8) in the region $t<0$. A trajectory with an intercept of -0.6 or higher and a slope of 0.9 would give rise, for example, to a vector meson with a mass of 1.33 GeV/c^2 or lower and strangeness $+2$. Such a particle would decay into KK or $KK\pi$. No such resonance has been observed.[20] The present data seem dominated by cut exchange, and they provide an additional argument against there being a low-mass (<1.33 GeV/c^2) strangeness-2 vector meson.[21]

C. Constituent-interchange model

The simplified constituent-interchange model[11] (CIM) has been successful in describing previous data for 200-GeV Λ and $\bar{\Lambda}$ production at small transverse momenta.[22]

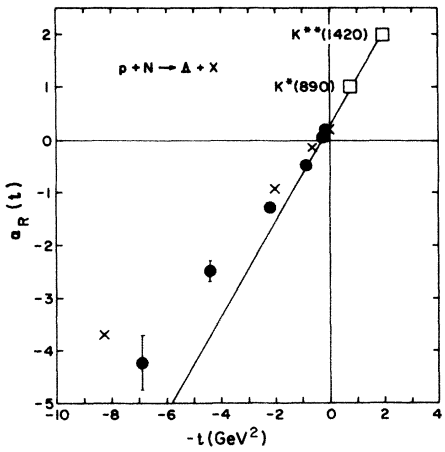

FIG. 24. Chew-Frautchi plot of $\alpha_R(t)$ from the Regge fit vs t for the Λ data of the present experiment (circles) compared to the 300-GeV data of Ref. 10 (crosses). The line is a function $\alpha_R(t)=0.25+0.9t$.

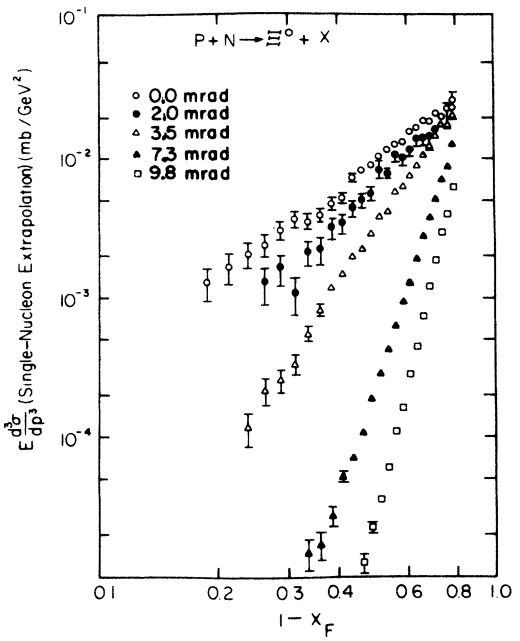

FIG. 25. Invariant cross sections for $\bar{\Xi}^0$ production from the "nucleon" target, obtained by extrapolation of the complex nuclear cross sections to $A=1$ via Eq. (4), plotted for fixed production angle vs $\ln(1-x)$, illustrating the validity of Eq. (6). The approximate linearity for small values of $(1-x)$ suggests triple-Regge behavior.

For the reaction $a+b\to c+$ anything at $p_t=0$, this version of the model predicts

$$E\,d^3\sigma/dp^3=R(1-x)^F\,. \tag{11}$$

The exponent F can be calculated from a product of factors which depend on the fate of the quarks in the incident projectile for the reaction $a\to c$. Each quark in the transition, $(q_1,q_2,q_3)\to(q_1',q_2',q_3')$, contributes a factor $(1-x)^{2n-1}$, where $n=$net flavor of $(q_i,\bar{q}_f)$. Hence if the quark is unchanged between a and c, multiply by $(1-x)^{-1}$. If the quark changes flavor from a to c, multiply by $(1-x)^3$; and if the quark dies, multiply by $(1-x)$. A comparison between Eq. (11) and Eq. (5) gives the relation between Regge and constituent-interchange models

$$F=1-2\alpha_R(0)\,. \tag{12}$$

Table IX gives values of F from empirical fits to data from the reactions $p\to\Xi^0$, $p\to\bar{\Xi}^0$, $p\to\Lambda$, and $p\to\bar{\Lambda}$ (the coefficient C_8 for Be given in Tables VII and VIII), and the Regge extrapolation results discussed in Sec. IV B. These two different methods of extracting the power of $(1-x)$ from the data differ by less than one unit in the Λ and Ξ^0 cases where they can be compared. Tables VII and VIII also show that C_8 is not a strong function of target material. The predictions of the CIM give the correct trend of F with produced particle and adequate numerical agreement for Λ and $\bar{\Lambda}$, where the numbers obtained here are consistent with earlier ones of Ref. 22. The CIM prediction for Ξ^0 and $\bar{\Xi}^0$ production disagree with the data by two units in F, which appears to be outside the uncertainties in extracting F from the data. The powers of $(1-x)$ obtained from the data via the functional fits and the Regge extrapolation are in fair agreement with each other. The trend of the results follows the predictions of Eq. (11), and the agreement is good for Λ and $\bar{\Lambda}$, where the numbers obtained here are consistent with the earlier measurements of Ref. 22.

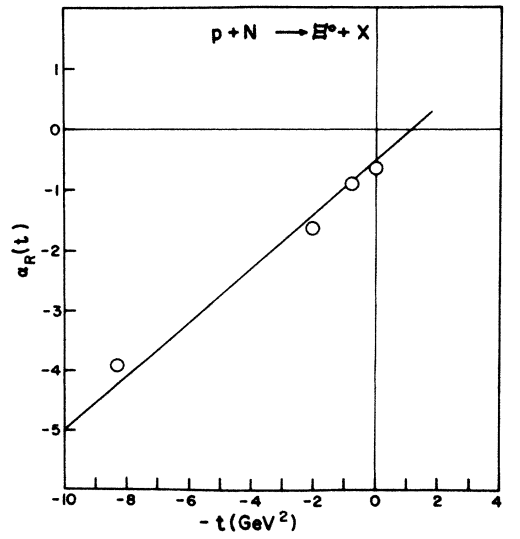

FIG. 26. Chew-Frautchi plot for $p+N\to\Xi^0+X$. The line represents the function $\alpha(t)=-0.5+0.45t$ which is expected if exchange of two K^*'s dominates the process.

D. Quark-recombination model

The quark-recombination model of Das and Hwa[9] can be extended to fragmentation of baryons into baryons and compared to the $p\to\Xi^0$ spectrum. In its simplest form, this model, in contrast with the triple-Regge model, has no dependence on transverse momentum. The differential multiplicity as a function of x is written as an integral over the product of two functions:

TABLE IX. Comparison of the Be data to the CIM and the triple-Regge model.

Reaction	F (CIM) Eq. (11)	C_8 from Tables VII and VIII	Regge $1-2\alpha_R(0)$
$p\to\Xi^0$	5	3.00±0.01	2.4±0.1
$p\to\bar{\Xi}^0$	9	11.0±0.1	
$p\to\Lambda$	1	0.86±0.04	0.50±0.05
$p\to\bar{\Lambda}$	9	8.4±0.2	

$$(x/\sigma_a)d\sigma/dx = \int_0^x (dx_1/x_1) \int_0^{x-x_1} (dx_2/x_2) \int_0^{x-x_1-x_2} (dx_3/x_3) F(x_1,x_2,x_3) R(x_1,x_2,x) , \quad (13)$$

where the quark distribution function appropriate to $p \rightarrow \Xi^0$ is

$$F(x_1,x_2,x_3) = \alpha x_1 u(x_1) x_2 s(x_2) x_3 s(x_3) \times (1-x_1-x_2-x_3) , \quad (14)$$

and the recombination function is

$$R(x_1,x_2,x_3,x) = \beta(x_1,x_2,x_3/x^3) \times \delta\left[\frac{x_1}{x}+\frac{x_2}{x}+\frac{x_3}{x}-1\right] . \quad (15)$$

Here α and β are both constants, and $xu(x)$ and $xs(x)$ are the valence u-quark and sea s-quark structure functions of Field and Feynman[23] and Duke and Taylor,[24] respectively.

The process described by Eq. (13) is one in which a $\Xi^0(uss)$ with momentum fraction x is formed by a spectator u quark with momentum fraction x_1 combining with two s quarks from the projectile sea with momentum fractions x_2 and x_3, respectively. Momentum conservation requires $x = x_1+x_2+x_3$. The extra factor of $(1-x_1-x_2-x_3)$ is a phase-space factor, while the first term in the recombination function favors $x_1 = x_2 = x_3 = x/3$. The differential multiplicity $(x/\sigma_a)(d\sigma/dx)$ is defined in terms of the invariant cross section by

$$(x/\sigma_a)(d\sigma/dx) = (\pi/\sigma_a) \int dp_t^2 (E\, d^3\sigma/dp^3) . \quad (16)$$

The model should be valid for $p+p \rightarrow \Xi^0$ + anything, but the data presented here are from complex nuclei. There are two ways to proceed. The Be target is thin in the A-dependence sense, so that a direct comparison of Eq. (13) with the Be cross section might be valid. On the other hand, an A-dependent extrapolation via Eq. (4) has been done as described by Eq. (3) with results shown in Table VIII, and this shape can be compared to Eq. (13). The quark structure functions have been empirically determined from other experimental data on meson production,[23,24] so that the recombination model formula can be evaluated apart from an overall normalization constant $\alpha\beta$.

Figure 27 shows the function $x(d\sigma/dx)$ obtained by integrating the fits in Table VII over p_t^2 for Be and the extrapolated nucleon compared to the calculated values from Eq. (13). To normalize the quark model curves, $\alpha\beta = 0.83$, $\sigma_a(\text{Be}) = 216$ mb (Ref. 25), and $\sigma_a(A=1) = 47$ mb were used. This value of the pp cross section was obtained by extrapolating Eq. (17) below to $A = 1$, which exceeds the true pp cross section (33 mb). The calculated spectrum follows the Be data very closely, but is a bit steeper than the extrapolated nucleon curve. Since the shape of the Be curve is probably a better indication of the

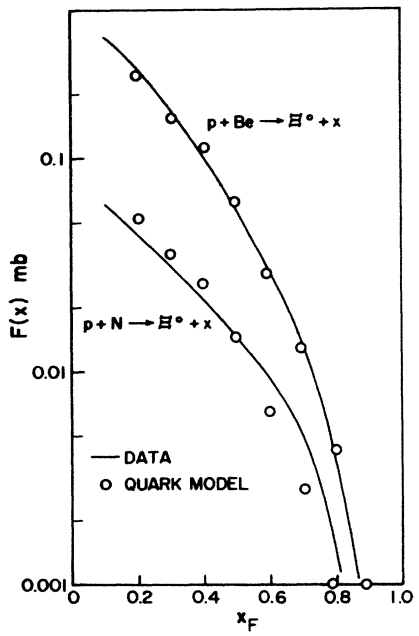

FIG. 27. Cross section for $p+\text{Be} \rightarrow \Xi^0$ and the extrapolated nucleon cross section, integrated over transverse momentum: $F(x) = \pi \int dp^2 (E\, d^3\sigma/dp^3)$. The open circles are the quark-recombination model calculations via Eq. (11).

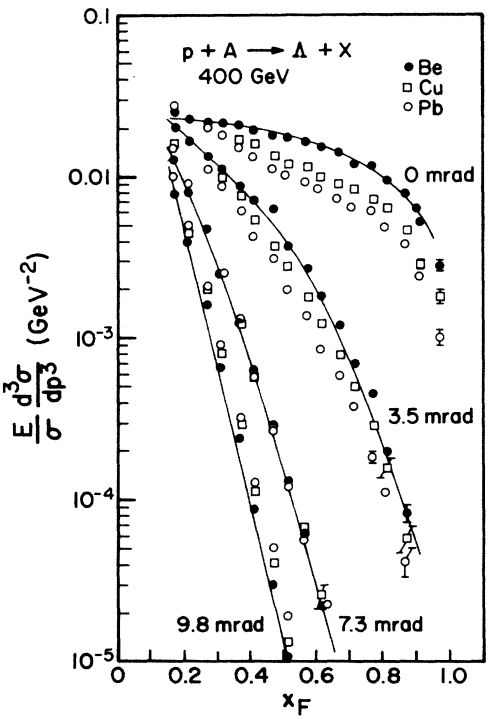

FIG. 28. Invariant cross sections for Λ production for the three targets divided by the appropriate absorption cross sections, to display the A dependence. Note that the Pb cross section is smaller than the Be at small angles, but larger at large angles. They are the fits of Table VIII for the Be data.

true hydrogen cross-section shape than is the extrapolated shape,[26] the data can be judged in agreement with the quark-recombination model of projectile fragmentation.

E. A dependence of the quark model

Figures 28 and 29 show the Λ and Ξ^0 cross sections for the three targets divided by the appropriate total absorption cross sections $\sigma_a(\mathrm{Be})=216$ mb, $\sigma_a(\mathrm{Cu})=812$ mb, and $\sigma_a(\mathrm{Pb})=1930$ mb. These values come from the measurements of Denisov *et al.*,[25] and were also used in Ref. 7. Since the absorption cross section depends on A according to the formula

$$\sigma_a(A)=A^{0.69}\sigma_a(A=1)\,, \tag{17}$$

a comparison of the various invariant cross sections plotted in this way displays the difference between the exponent $\alpha(x,p_t)$ in Eq. (4) and 0.69. Note that the small angle cross sections in Fig. 28 become smaller as A increases, but that the trend reverses at 9.8 mrad. The Ξ^0 cross sections for Be, Cu, and Pb are plotted versus A in Fig. 30 for four different (x,p_t). The slopes of these lines are $\alpha(x,p_t)$.

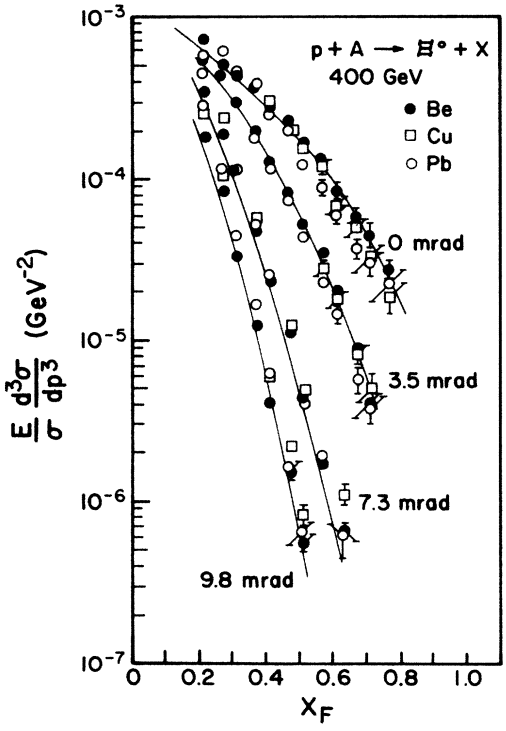

FIG. 29. Invariant cross sections for Ξ^0 production for the three targets divided by the appropriate absorption cross sections, to display the A dependence. The Pb yield is again smaller than the Be yield at small angles, although the A dependence of the cross section is closer to the absorption cross section than in the Λ case (Fig. 28). The lines are the fits of Table VII to the Be data.

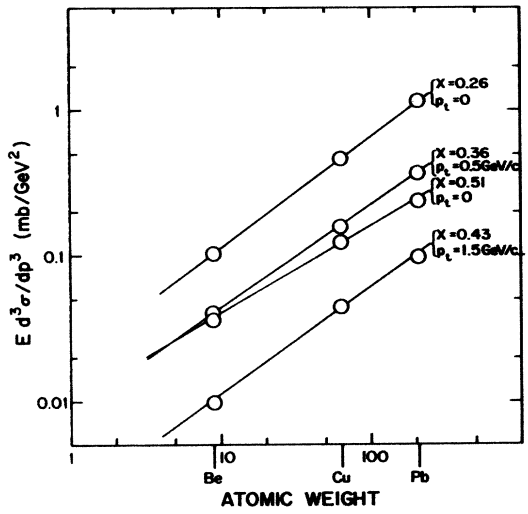

FIG. 30. Log-log plot of the Ξ^0 cross sections at selective (x,p_t) values, showing that the power-law hypothesis of Eq. (4) is consistent with the data from the three targets.

Values of the exponent $\alpha(x,p_t)$ obtained in this way are given as a function of p_t for various values of x in Fig. 31 for Ξ^0 and in Fig. 32 for Λ. A plot similar to Fig. 32 for 300-GeV production appeared in Ref. 7. The exponent increases with increasing p_t at constant x, indicating that the yield at large p_t in a heavy nucleus is enhanced over that in a light nucleus. The general trends in the Λ and Ξ^0 data are the same, although α tends to be a bit larger in the Ξ^0 case. This is particularly apparent in Fig. 33, where the exponent $\alpha(x)$, defined by

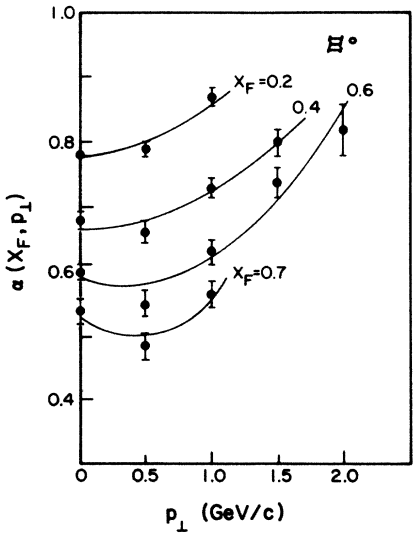

FIG. 31. The exponent $\alpha(x,p_t)$ from the slopes of the lines of Fig. 30, plotted vs p_t for fixed values of x.

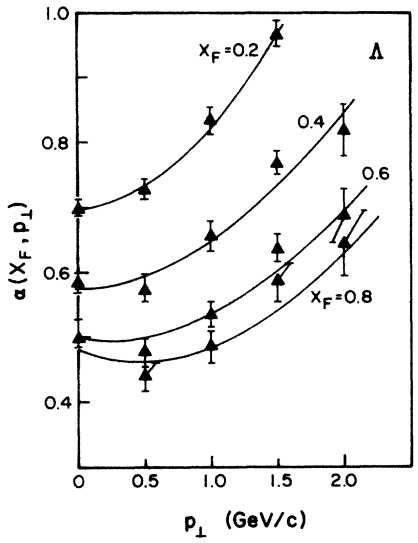

FIG. 32. The same as Fig. 31 except for Λ's. A similar graph for 300-GeV Λ production is shown in Ref. 6.

$$x\, d\sigma(A)/dx = A^{\alpha(x)} x\, d\sigma(A=1)/dx\ , \tag{18}$$

is plotted for a number of different particles. The K_S^0 and $\bar{\Lambda}$ data are for 300-GeV production taken from Ref. 6. The invariant cross sections given by the fits of Tables VII and VIII were integrated over p_t^2 using Eq. (14) to obtain functions of x alone.

As mentioned in the Introduction, it was first recognized by Busza[12] that $\alpha(x)$ has nearly the same form for a wide variety of different particles (see Fig. 33), and that such a similarity is inconsistent with any simple collision

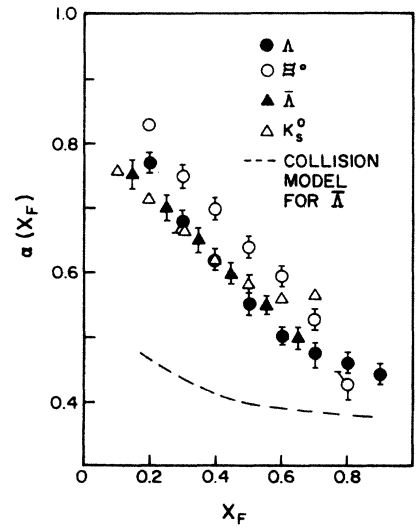

FIG. 33. The exponent $\alpha(x)$ defined by Eq. (18) for Λ and Ξ^0 from this experiment compared to the 300-GeV data of Ref. 6 for $\bar{\Lambda}$ and K_S^0. The predictions of the simple collision model for Λ (not shown) are in good agreement with the data, whereas the predictions for $\bar{\Lambda}$ (dashed line) disagree significantly.

model like that of Ref. 7 in which the only effect of a thick nucleus is the straggling of a single forward-moving hadronic system. The problem with such models is that they contain only one parameter, independent of the final-state particle observed, and thus necessarily predict different attenuations in a heavy nucleus for different inclusive spectrum shapes. Thus, while the model yields results for $p\to\Lambda$ which are in good agreement with the data, a steeply falling cross section with increasing x, like $p\to\bar{\Lambda}$, would have a more slowly varying $\alpha(x)$, because there are no high x particles to straggle down and pile up at low x. In this latter case, the prediction of the model, shown in Fig. 33, is totally inconsistent with the data. Therefore, simple collision models must be discarded.

Nevertheless, the phenomenon of forward attenuation, i.e., lower α at high x_F, of the particles in a heavy nucleus makes some sort of collision model very attractive. Several authors have extended the collision idea to the quark level with some success. These data for $p\to\Xi^0$ have been analyzed in this way by Takagi,[15] as have the earlier data of Ref. 6 by Dar and Takagi[14] and Bialas and Bialas.[13] Very good fits to the A-dependent spectra were obtained using a cross section of the form

$$(x/\sigma_a)(d\sigma/dx) = P_A^{(1)} g^{(1)}(x) + P_A^{(2)} g^{(2)}(x) + P_A^{(3)} g^{(3)}(x)\ . \tag{19}$$

Here the coefficients $P^{(1)}$, $P^{(2)}$, and $P^{(3)}$ are A-dependent probabilities that one, two, or three quarks in the incident proton interact (are "wounded") in passing through the nucleus, and the distribution functions $g(x)$ are A independent. The P's satisfy the sum

$$P_A^{(1)} + P_A^{(2)} + P_A^{(3)} = 1\ , \tag{20}$$

and $P^{(1)}=1$ for a single-nucleon target. An optical model and the additive quark model were used in Ref. 15 to calculate fixed values of the $P^{(i)}$, while

$$g^{(i)}(x) = c^{(i)} x^{a^{(i)}} (1-x)^{b^{(i)}}$$

were functions fitted from the experimental spectrum shapes. The probability $P^{(3)}$ was small for all A, and was ignored, so that the three targets over-constrained the model, giving a χ^2 test for goodness of fit which was satisfactory both for Λ and Ξ^0. The functions $g^{(1)}$ and $g^{(2)}$ were, of course, different for the two hyperons. In the model $g^{(1)}(x)$ is the production spectrum from hydrogen, and should be calculable from a quark-recombination model formula similar to Eq. (11).

Table X, adapted from Ref. 17, gives the parameters obtained by fitting the $p\to\Lambda$ and $p\to\Xi^0$ data to Eq. (19). These fits are compared to the Be and Pb data in Fig. 34. The agreement is quite good. The functions $g^{(2)}(x)$ fall off faster with increasing x than do the $g^{(1)}(x)$, as would be expected for an extra quark interaction.

Hwa in Ref. 16 applies a collision picture similar to that of Ref. 7 to the A dependence of $p+A\to p+$ anything, and suggests the possibility of using such a collision function on the quark level in a way which should, in principle, allow the calculation of all of the functions $g^{(i)}(x)$ in Eq. (19) above. The picture is a combination of

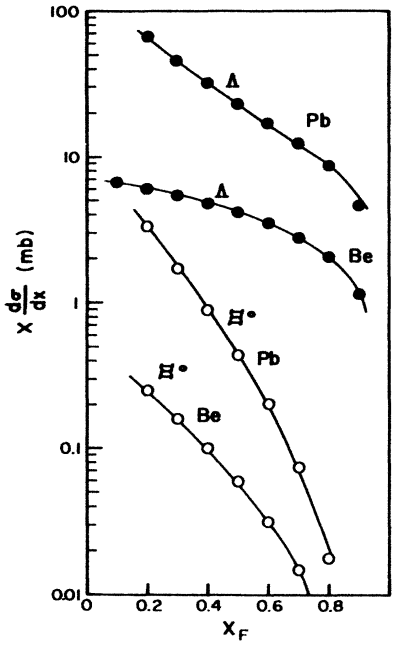

FIG. 34. "Wounded"-quark A-dependence model calculations for $p\to\Lambda$ and $p\to\Xi^0$. The open circles are from the fits given in Table X, and the lines are from the experimental data.

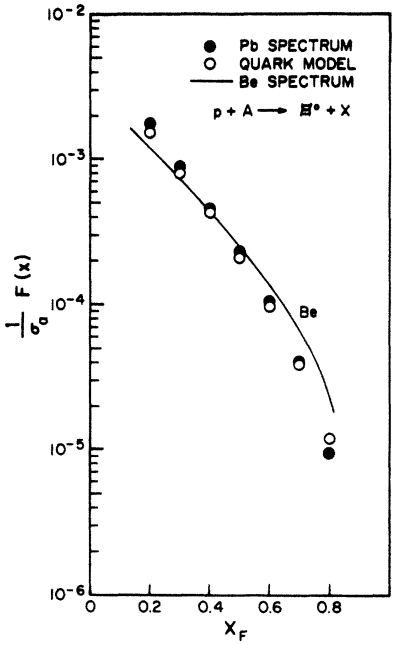

FIG. 35. Straggling-function calculations of Ξ^0 A dependence. The Pb cross section was calculated from the Be cross section via Eq. (22) with $\lambda=0.33$.

the wounded quarks plus the recombination model. In going through the nucleus, the projectile fragments into the quarks necessary to form the final-state particle observed, and these quarks scatter and straggle as they leave the nucleus. The recombination to form the final-state particle occurs well outside the nucleus, and is A independent. The collision function adopted in Ref. 16 is

$$Q(z)=\lambda z+(1-\lambda)\delta(x-1)\,, \tag{21}$$

where $z=x/x'$ is the ratio of x after collision to x before the collision, and $\lambda=0$ would correspond to no straggling ($z=1$).

If Eq. (11) above is assumed to apply to a complex nucleus, then the recombination function R should be A independent, but the quark distribution function F will be changed in a heavy nucleus by the collisions of the outgoing quarks, which are described by Eq. (21). If, in nucleus A, a quark suffers one extra collision relative to hydrogen, then the spectrum shape for this nucleus could be calculated in terms of the shape for $A=1$ by modifying the function F in the following manner:

$$F_A(x_1,x_2,x_3)=\int_{x_1}^1(dx_1'/x_1')\int_{x_2}^1(dx_2'/x_2')\int_{x_3}^1(dx_3'/x_3')F(x_1',x_2',x_3')Q(x_1/x_1')Q(x_2/x_2')Q(x_3/x_3')\,. \tag{22}$$

This function, substituted into Eq. (13), should give $(x/\sigma_a)(d\sigma/dx)$. The mean number of collision suffered by a quark in nuclear matter is given by the formula $\bar{\nu}_{qA}=A\sigma_{qp}/\sigma_{qA}$. The additive quark model gives $\sigma_{qp}=\sigma_{pp}/3=11$ mb, and the optical model is used in Ref. 15 to calculate $\sigma_{q\mathrm{Be}}=80$ mb, $\sigma_{q\mathrm{Cu}}=400$ mb, and $\sigma_{q\mathrm{Pb}}=1050$ mb, all of which combine to give $\bar{\nu}_{q\mathrm{Be}}=1.2$, $\bar{\nu}_{q\mathrm{Cu}}=1.75$, and $\bar{\nu}_{q\mathrm{Pb}}=2.2$. Thus, on the average a quark suffers one extra collision in Pb relative to Be.

In Sec. IV C the structure functions $xu(x)$ from Ref. 23 and $xs(x)$ from Ref. 24 were applied via Eqs. (11) and (12) to the $p+\mathrm{Be}\to\Xi^0$ spectrum and the model is quite good. The agreement at high x, where the A-dependence effects are largest, was improved by using $xs(x)=0.135(1-x)^5$ instead of $(1-x)^{5.75}$ of Ref. 23. With this modification in Eq. (14), Eq. (22) was used to calculate $F_{\mathrm{Pb}}(x_1,x_2,x_3)$ with g a free parameter, and a χ^2 fit to the lead spectrum shape was performed.

TABLE X. Results of applying the quark models to forward hyperon A dependence (adapted from Ref. 17).

$$x\frac{d\sigma}{dx}=\sigma_a[P^{(1)}g^{(1)}(x)+P^{(2)}g^{(2)}(x)]$$

Target	σ_a (mb)[a]	A-dependent coefficients $P^{(1)}$[b]	$P^{(2)}$[b]
Be	216	0.846	0.146
Cu	812	0.585	0.347
Pb	1930	0.421	0.432

Particle	A-independent functions $g^{(1)}(x)$	$g^{(2)}(x)$	χ^2/DF[c]
Λ	$0.0521x^{0.38}(1-x)^{0.9}$	$0.26x^{0.23}(1-x)^{5.2}$	0.1
Ξ	$0.0016(1-x)^{2.59}$	$0.0098(1-x)^{5.29}$	0.1

[a]Taken from Ref. 25.
[b]Taken from Ref. 15.
[c]For the Be fit.

The results of this calculation gave λ in Eq. (21): $\lambda=0.33$ with a $\chi^2=13.4$ for 30 degrees of freedom. The overall normalization constant used was $\alpha\beta=0.65$, slightly different from 0.83 in Fig. 27 because of the different shape of $xs(x)$. The fits compared to the Be and Pb data are shown in Fig. 35. The agreement is quite good.

In Ref. 16 Hwa found $\lambda=0.43$ fit the $p+A\rightarrow p+X$ spectra best, where λ referred to proton rather than quark straggling. The results obtained here show that the quarks in $p\rightarrow\Xi^0$ prefer to straggle a bit less.

In conclusion, the quark-model picture of forward A dependence describes the data satisfactorily. The correspondence between the wounded-quark expansion of Eq. (19) and the collision-function approach of Eq. (22) could be made by adopting the basic function $F(x_1,x_2,x_3)$ for hydrogen, and then casting the collision expression in continuous form so that it is valid for any nucleus. In this way the functions $g^{(i)}(x)$ should be calculable. The expansion of Eq. (22) in powers of λ shows the expected trend, that more quark collisions lead to a steeper falloff in $(1-x)$.

ACKNOWLEDGMENTS

We gratefully acknowledge the help of the staff of Fermilab, in particular the Meson Lab, during this experiment. Much of the apparatus was designed and built by E. Behr, S. Fraser, J. Jaske, and G. Ott. D. Mills assisted with the data taking. One of us (T.D.) wishes to thank the Aspen Center for Physics where parts of this paper were written. This work was supported in part by the National Science Foundation, and by the Department of Energy.

---

*Present address: Honeywell Corp., MN38-1500, 10400 Yellow Circle Dr., Minnetonka, MN 55343.

†Present address: MS221, Fermilab, P.O. Box 500, Batavia, IL 60510.

‡Present address: MS219, Fermilab, P.O. Box 500, Batavia, IL 60510.

§Present address: Physics Department, Univ. of Oklahoma, Norman, OK 73019.

**Present address: Physics Department, Rockefeller Univ., New York, NY 10021; Mailing address: CERN, CH-1211, Geneve 23, Switzerland.

††Now at Fonar Corp., Melville, NY 11747.

‡‡Present address: Salomon Brothers, Inc. 41st Floor, 1 New York Plaza, New York, NY 10004.

[1]R. Handler *et al.*, Phys. Rev. D **25**, 639 (1982).

[2]P. T. Cox *et al.*, Phys. Rev. Lett. **46**, 877 (1981).

[3]K. Heller *et al.*, Phys. Rev. Lett. **51**, 2025 (1983).

[4]L. Pondrom *et al.*, in *Proceedings of the Xth International Symposium on Multiparticle Dynamics, Goa, India, 1979*, edited by S. N. Gauguli, P. K. Malhotra, and A. Subramanian (Tata Institute, Bombay, 1980), p. 579.

[5]L. Pondrom *et al.*, in *VI International Seminar on Problems in High Energy Physics, Dubna, USSR, 1981*, edited by A. M. Baldin (Dubna, USSR, 1982), p. 181.

[6]P. Skubic *et al.*, Phys. Rev. D **18**, 3115 (1978).

[7]K. Heller *et al.*, Phys. Rev. D **16**, 2737 (1977).

[8]See, for example, P. D. B. Collins, *An Introduction to Regge Theory and High Energy Physics* (Cambridge University Press, Cambridge, England, 1977).

[9]K. P. Das and R. C. Hwa, Phys. Lett. **68B**, 459 (1977).

[10]T. J. Devlin *et al.*, Nucl. Phys. **B123**, 1 (1977).

[11]R. Blankenbecler and S. J. Brodsky, Phys. Rev. D **10**, 2973 (1974).

[12]W. Busza, in *Multiparticle Dynamics 1982*, edited by W. Kittel, W. Metzger, and A. Stergiou (World Scientific, Singapore, 1983), p. 367. See also D. S. Barton *et al.*, Phys. Rev. D **27**, 2580 (1983).

[13]A. Bialas and E. Bialas, Phys. Rev. D **20**, 2854 (1979).

[14]A. Dar and F. Takagi, Phys. Rev. Lett. **44**, 768 (1980).

[15]F. Takagi, Phys. Rev. D **27**, 1461 (1983).

[16]R. Hwa, Phys. Rev. Lett. **52**, 492 (1984).

[17]L. Pondrom, Phys. Rep. **122**, 57 (1985).

[18]Particle Data Group, Rev. Mod. Phys. **55**, S1 (1984).

[19]M. Bourquin *et al.*, Z. Phys. C **5**, 275 (1980).

[20]H. Lipkin, Phys. Rev. D **7**, 2262 (1973).

[21]The same remarks apply to any other $S=2$ states on the same Regge trajectory. One example would be a scalar meson with a mass of 0.8 GeV/c or lower. Such a state, which would be stable against strong decay, has not been observed.

[22]R. T. Edwards *et al.*, Phys. Rev. D **18**, 76 (1978).

[23]R. D. Field and R. P. Feynman, Phys. Rev. D **15**, 2590 (1977).

[24]Dennis Duke and Frank Taylor, Phys. Rev. D **17**, 1788 (1978).

[25]S. P. Denisov *et al.*, Nucl. Phys. **B61**, 62 (1973).

[26]This assertion is true for $p\rightarrow\Lambda$, $p\rightarrow K_S^0$, and $p\rightarrow\bar{\Lambda}$, for which hydrogen data are available. See R. Grobel, Ph.D. thesis, University of Wisconsin, 1980.